The Astrophysical Journal, 791:17 (17pp), 2014 August 10 doi:10.1088/0004-637X/791/1/17
© 2014. The American Astronomical Society. All rights reserved. Printed in the U.S.A.

THE NATURE OF EXTREME EMISSION LINE GALAXIES AT $z = 1$–2: KINEMATICS AND METALLICITIES FROM NEAR-INFRARED SPECTROSCOPY*

Michael V. Maseda[1], Arjen van der Wel[1], Hans-Walter Rix[1], Elisabete da Cunha[1], Camilla Pacifici[2], Ivelina Momcheva[3], Gabriel B. Brammer[4], Sharon E. Meidt[1], Marijn Franx[5], Pieter van Dokkum[3], Mattia Fumagalli[5], Eric F. Bell[6], Henry C. Ferguson[4], Natascha M. Förster-Schreiber[7], Anton M. Koekemoer[4], David C. Koo[8], Britt F. Lundgren[9], Danilo Marchesini[10], Erica J. Nelson[3], Shannon G. Patel[11], Rosalind E. Skelton[12], Amber N. Straughn[13], Jonathan R. Trump[14], and Katherine E. Whitaker[13]
[1] Max-Planck-Institut für Astronomie, Königstuhl 17, D-69117 Heidelberg, Germany; maseda@mpia.de
[2] Yonsei University Observatory, Yonsei University, Seoul 120-749, Korea
[3] Department of Astronomy, Yale University, New Haven, CT 06520, USA
[4] Space Telescope Science Institute, 3700 San Martin Drive, Baltimore, MD 21218, USA
[5] Leiden Observatory, Leiden University, Leiden, The Netherlands
[6] Department of Astronomy, University of Michigan, 500 Church Street, Ann Arbor, MI 48109, USA
[7] Max-Planck-Institut für extraterrestrische Physik, Giessenbachstrasse 1, D-85748 Garching, Germany
[8] UCO/Lick Observatory and Department of Astronomy and Astrophysics, University of California Santa Cruz, 1156 High Street, Santa Cruz, CA 95064, USA
[9] Department of Astronomy, University of Wisconsin, 475 North Charter Street, Madison, WI 53706, USA
[10] Physics and Astronomy Department, Tufts University, Robinson Hall, Room 257, Medford, MA 02155, USA
[11] Carnegie Observatories, 813 Santa Barbara Street, Pasadena, CA 91101, USA
[12] South African Astronomical Observatory, P.O. Box 9, Observatory 7935, Cape Town, South Africa
[13] Astrophysics Science Division, Goddard Space Flight Center, Code 665, Greenbelt, MD 20771, USA
[14] Department of Astronomy and Astrophysics, The Pennsylvania State University, Davey Lab, University Park, PA 16802, USA
Received 2014 January 17; accepted 2014 June 20; published 2014 July 21

ABSTRACT

We present near-infrared spectroscopy of a sample of 22 Extreme Emission Line Galaxies at redshifts $1.3 < z < 2.3$, confirming that these are low-mass ($M_\star = 10^8$–$10^9\ M_\odot$) galaxies undergoing intense starburst episodes ($M_\star$/SFR $\sim$ 10–100 Myr). The sample is selected by [O III] or Hα emission line flux and equivalent width using near-infrared grism spectroscopy from the 3D-HST survey. High-resolution NIR spectroscopy is obtained with LBT/LUCI and VLT/X-SHOOTER. The [O III]/Hβ line ratio is high ($\gtrsim$5) and [N II]/Hα is always significantly below unity, which suggests a low gas-phase metallicity. We are able to determine gas-phase metallicities for seven of our objects using various strong-line methods, with values in the range 0.05–0.30 $Z_\odot$ and with a median of 0.15 $Z_\odot$; for three of these objects we detect [O III] λ4363, which allows for a direct constraint on the metallicity. The velocity dispersion, as measured from the nebular emission lines, is typically $\sim$50 km s^{-1}. Combined with the observed star-forming activity, the Jeans and Toomre stability criteria imply that the gas fraction must be large ($f_{\rm gas} \gtrsim 2/3$), consistent with the difference between our dynamical and stellar mass estimates. The implied gas depletion timescale (several hundred Myr) is substantially longer than the inferred mass-weighted ages ($\sim$50 Myr), which further supports the emerging picture that most stars in low-mass galaxies form in short, intense bursts of star formation.

Key words: galaxies: dwarf – galaxies: evolution – galaxies: formation – galaxies: high-redshift – galaxies: starburst

Online-only material: color figures

1. INTRODUCTION

The life cycles of dwarf galaxies with present-day stellar masses $\lesssim 10^9\ M_\odot$ illustrate many challenges to our current understanding of galaxy formation and evolution. While we see that starbursts do not play an important role in the global star-formation at the present epoch (Lee et al. 2009), it is likely that the star formation histories of dwarf galaxies are complex and varied (Mateo 1998) and that their typical star formation rates (SFRs) were higher in the past (e.g., Gallagher et al. 1984). That star formation in low-mass galaxies may be very burst-like is predicted by hydrodynamical simulations (e.g., Pelupessy et al. 2004; Stinson et al. 2007; Shen et al. 2013). In general, star formation appears to be regulated by stellar feedback in the form of supernovae and winds that heat and deplete the central reservoirs of cold gas required for continued star formation. In simulations of lower mass systems, feedback is predicted to eject gas out of the galaxy and into the halo, resulting in an episodic star formation history across the entire galaxy (Stinson et al. 2007). Repeated bursts have been cited as the driving force behind intense feedback mechanisms that can change the dynamical profile of the systems by driving baryons out of the center of the halo on short timescales, which also displaces the dark matter from the center and creates a cored dark matter profile (Navarro et al. 1996; Pontzen & Governato 2012; Governato et al. 2012; Zolotov et al. 2012; Amorisco et al. 2014), potentially addressing one of the principal challenges to the standard ΛCDM cosmology.

Until recently, however, the progenitors of contemporary dwarf galaxies at high redshift could not be studied directly.

* This work is based on observations taken by the 3D-HST Treasury Program and the CANDELS Multi-Cycle Treasury Program with the NASA/ESA *HST*, which is operated by the Association of Universities for Research in Astronomy, Inc., under NASA contract NAS5-26555. X-Shooter observations were performed at the European Southern Observatory, Chile, Program 089.B-0236(A).

"Archaeological" studies of resolved stellar populations in local dwarfs (e.g., Grebel 1997; Weisz et al. 2011) have confirmed that their star-formation histories are indeed not smooth, and have also found that a large fraction of their stars formed at early epochs ($z > 1$). For such old stellar populations (>7 Gyr), the age resolution achieved by the archaeological approach is insufficient to distinguish star formation events with durations of 10^7 and 10^8 yr, leaving the actual "burstiness" of the star formation history unconstrained.

Look-back studies, directly observing the star formation activity in very low-mass systems at $z > 1$, were impractical until recently. However, near-infrared spectroscopy and deep imaging from the Wide-field Camera 3 (WFC3) on the *Hubble Space Telescope* (*HST*) has provided a new opportunity. An abundant population of galaxies at $z \sim 1.7$ with extremely high equivalent widths (EWs) was found by van der Wel et al. (2011) using data from the Cosmic Assembly Near-infrared DEep Legacy Survey[15] (CANDELS; Grogin et al. 2011; Koekemoer et al. 2011). They find a large number of objects with unusual $I-J$ and $J-H$ colors which imply the presence of a bright emission line in the J-band, likely to be [O III] after considering other photometric constraints. Slitless grism spectroscopy confirms the redshifts and emission-line interpretation of four of these objects. These are the high-EW tail of the emission line galaxies found in Straughn et al. (2008) via slitless grism spectroscopy at *HST*, a tail which is also probed by Atek et al. (2011). Other objects with similarly low masses and metallicities at these redshifts have been discovered in Brammer et al. (2012b; $EW_{[O\,III],rest} = 1499$ Å) and van der Wel et al. (2013; $EW_{[O\,III],rest} = 1200$ Å) assisted by strong gravitational lensing, in Masters et al. (2014; $EW_{[O\,III],rest} = 154$ Å), in Erb et al. (2010; $EW_{[O\,III],rest} = 285$ Å), and in Maseda et al. (2013; discussed further below). All of these objects are emission-line dominated systems with low metallicities and high equivalent widths, the so-called "Extreme Emission Line Galaxies" (EELGs).

These systems are likely the high-EW tail of the distribution of high-redshift dwarf galaxies and resemble the class of blue compact dwarf galaxies (BCDs; Sargent & Searle 1970) observed locally in several ways: low masses, high SFRs relative to their mass, and strong emission lines. However, the EELGs are indeed "extreme," with specific star formation rate (sSFR) values an order of magnitude higher than the BCDs, similar to the strong [O III] emitters ("green peas") discovered photometrically in the Sloan Digital Sky Survey (SDSS) by Cardamone et al. (2009), as well as spectroscopically by Amorín et al. (2010) and Izotov et al. (2011). As suggested by those authors, the star-formation mode exhibited in the "green peas" is likely a relic of a mode that was much more prevalent in the earlier universe: their comoving number density is one to two orders of magnitude lower than the value of 3.7×10^{-4} Mpc^{-3} for EELGs at $z \sim 1.7$ (van der Wel et al. 2011).

The implication of strong emission lines and an extremely faint continuum are that these systems have low masses and are undergoing an intense burst of star formation. Equivalent widths >100 Å and stellar masses of 10^8–10^9 $M_\odot$ imply sSFRs in excess of 10 Gyr^{-1}, which is more than an order of magnitude higher than star-forming systems of equivalent masses at lower redshifts (Karim et al. 2011). These low stellar and dynamical masses are confirmed in Maseda et al. (2013), who also rule out significant contributions to the total mass from older stellar populations for objects with restframe [O III] λ5007 equivalent widths >500 Å and intimate that the bursts are intense and have low metallicities. The implied SFRs and masses have only been reproduced recently in hydrodynamical simulations (e.g., in Shen et al. 2013).

Although these previous observational studies have placed constraints on various quantities, many uncertainties remain. In the case of Maseda et al. (2013) and van der Wel et al. (2011), all of the observed [O III], Hβ, and Hα emission is attributed to star formation and not active galactic nuclei (AGNs). In van der Wel et al. (2011), upper limits are placed on the black hole masses from the UV-continuum slopes, but their starbursting nature is merely plausible given the lack of knowledge about low-metallicity AGNs (Izotov & Thuan 2008; Kewley et al. 2013). Low metallicies are simply inferred from the consistency of the spectral energy distribution (SED) fits using low-Z (0.2 $Z_\odot$) templates with the observed photometry.

These objects represent a field of growing importance, both for studies of low-mass dwarf galaxies and for the highest-z galaxies observed. Depending on the strength, duration, and initial mass of these bursts, the descendants could display a wide range of masses, from present-day $\sim 10^9$ $M_\odot$ dwarf galaxies to potentially Milky-Way-like systems, particularly if merging is important. In any case, these galaxies are also significant contaminants in searches for higher-z dropout sources (Atek et al. 2011), as in the case of *UDFj-30546284* (Ellis et al. 2013; Brammer et al. 2013; Bouwens et al. 2013). As mentioned in Atek et al. (2011) and Coe et al. (2013), great care must be taken in the interpretation of high-z candidates, as EELGs can potentially reproduce their observed colors (although the implied EWs in the latter case exceeded those that can be produced from star formation alone).

Some issues still remain in our understanding of such systems, such as stringent limits to the low masses and metallicities, including those with EWs < 500 Å, and the starburst origin of their strong emission lines. Here we combine both high- and low-resolution near-IR spectroscopy with broadband photometry. With the low-resolution spectra, we select candidates for follow-up high-resolution spectroscopy and obtain emission line fluxes. The high-resolution spectra constrain various emission line ratios, some of which are useful diagnostics of AGN activity, as well as line widths, which are themselves a probe of the dynamical masses of the systems. This provides strong evidence for their low masses and low metallicities, as well as confirming their starbursting nature. Sophisticated modeling of the broadband SEDs constrains the stellar masses and ages, as well as providing information on the dust content and metallicities. Together, this tells us about the strength and duration of the star-forming event.

The remainder of this paper is organized as follows. In Section 2, we describe the near-infrared spectroscopy and multi-band photometry used in the initial candidate selection process and the subsequent follow-up observations. Section 3 presents the results of the spectroscopic study, including emission-line widths, physical sizes, and masses. In Section 4, we confirm their low metallicities and rule out AGNs as a significant source of contamination. Section 5 presents the implications of this work for the gas content of these systems, and Section 6 summarizes our findings and puts the results into the overall context of the formation history of dwarf galaxies. We adopt a flat ΛCDM cosmology with $\Omega_m = 0.3$ and $H_0 = 70$ km s^{-1} Mpc^{-1} and a Chabrier (2003) initial mass function (IMF) throughout.

[15] http://candels.ucolick.org/

2. DATA

2.1. Candidate Selection

In order to search for and investigate these "starbursting dwarf galaxies," we take a multi-faceted approach. Our preliminary search utilizes data from the 3D-HST survey[16] (van Dokkum et al. 2011; Brammer et al. 2012a), a near-infrared spectroscopic Treasury program utilizing the WFC3. This program provides WFC3/IR primary and Advanced Camera for Surveys (ACS) parallel imaging and grism spectroscopy over approximately three-quarters (625 arcmin^2) of the CANDELS fields. The main source of spectroscopic data comes from the WFC3 G141 grism, with an effective wavelength coverage of 1.1 to 1.65 μm.

The grism data allow us to select and confirm strong line emitters spectroscopically. Photometric cuts, such as the *iJH* cut of van der Wel et al. (2011) and a similar *ViJH* selection (excess in *H* compared to a blue continuum, all from CANDELS), are used to preselect objects with strong features in their SEDs. The G141 grism data are reduced according to Brammer et al. (2012a) for the UKIDSS Ultra-Deep Survey (UDS), GOODS-South (GOODS-S), and COSMOS fields, and are then used to confirm bright lines with little or no associated continuum. While we find numerous examples of these objects at $z > 1$ (M. Maseda et al., in preparation), we focus here on objects where the emission lines do not fall in the wavelength range between the *J*-, *H*-, and *K*-bands, enhancing the chances for detectability from the ground. The low-resolution WFC3 grism data ($R \sim 130$) provide redshift information such that targets can be selected with [O III] in the redshift range $1.15 < z < 2.40$ and Hα in the redshift range $0.64 < z < 1.59$ to $\delta z/z \sim 0.005$. However, our photometric preselection relies on flux excesses such that we mostly see objects at $1.3 \lesssim z \lesssim 1.8$ and $2.1 \lesssim z \lesssim 2.3$. Note that we do not resolve the continuum in our ground-based observations (discussed presently), so all EW values are calculated from the grism spectra directly. In total, we select 31 objects for ground-based spectroscopic observations using this method. An additional five candidates are taken from the sample of van der Wel et al. (2011) and one from Straughn et al. (2011). Their equivalent widths as a function of redshift are shown in Figure 1. Non-detections are due to either intrinsic faintness in the lines or contamination from OH-skylines.

2.2. LBT/LUCI1 Spectroscopy

We observed our grism-selected sample with the LUCI1 multi-object spectrograph (Seifert et al. 2003) on the 8.4 m Large Binocular Telescope (LBT). We use LUCI1 in MOS mode, splitting our 31 candidates between four masks, during 2012 April (two masks in the COSMOS field), 2012 October (one mask in the UDS field), and 2013 March (an additional mask in the COSMOS field). Approximately two hours are spent observing in each of the *J*- and *H*-bands for the first two COSMOS masks (A and B) using 1″ slits, two hours in each of the *H*- and *K*-bands for the UDS mask (C) with 0.″6 slits, and three total hours on the final COSMOS mask (D) in the *J*- and *H*-bands using 0.″6 slits. All data are taken using the high-resolution 210_*zJHK* grating ($R_J = 8460$, $R_H = 7838$, $R_K = 6687$). The exposures are dithered by 3″ and are of varying durations, depending on the band: *J*-band data using 600 s exposures, *H*-band data with 300 s exposures, and *K*-band data with 120 s exposures. The shorter integrations in the *H*- and *K*-bands lead to lower signal-to-noise ratio (S/N) due to additional readnoise, but are necessary so as not to saturate the detector in the regions with the brightest OH sky lines. Seeing was generally good (between 0.″5 and 1″ in the optical) during the COSMOS observations, with good transparency. For the UDS observations, seeing was generally better than 1″. Table 1 details the observations of individual objects, including IDs (from the CANDELS catalogs, discussed in Section 3.1), coordinates, and the main line detections.

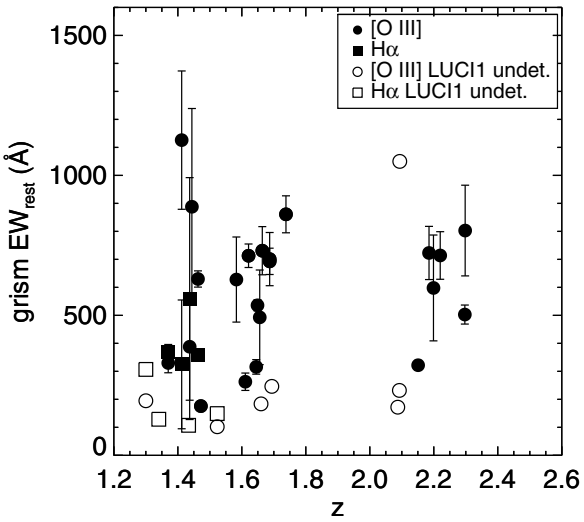

Figure 1. Restframe equivalent widths as a function of redshift for our entire sample. Circles represent equivalent widths from [O III]$_{5007}$ and squares represent equivalent widths from Hα. The equivalent widths were determined from photometry and grism spectroscopy, see Section 2.1. For objects in which both [O III] and Hα are visible in the grism spectrum, both equivalent widths are plotted. Open symbols show objects without LUCI1 line detections, due to intrinsic faintness or skyline contamination. Our emission-line detection rate is close to 100% for objects with EW > 300 Å.

2.2.1. LUCI1 Data Reduction

We first mask regions of the spectra that are affected by persistence due to the acquisition and alignment exposures. This effect is reduced with each readout, so we only mask the regions if they are 2σ higher than the background level. We then create flat-field images from lamp-illuminated exposures and remove cosmic rays using a median-stacking technique. The most important cosmetic step is the removal of bad pixels, which are identified in the lamp-illuminated exposures, and the hot pixels in the spectra, which are identified in dark exposures. Additionally, for an as-yet unknown reason, the first exposure of every series has small "halos" around the hot pixels. As such, we remove slightly larger regions around these hot pixels in the first exposure of every series. Our wavelength calibration is done using the OH sky lines, with a code based on `XIDL` routines.[17] We also use `XIDL` for the final sky subtraction, which uses a spline-fitting algorithm to measure and remove the lines. To maximize S/N, we do not use frame-frame subtraction and instead measure the sky from the individual frames, with the exception being some objects with particularly bad skyline contamination, where frame-frame subtraction better removes the skylines but adds noise to the spectrum. Dithering the exposures by 3″ ensures a decreased dependence on the pixel-to-pixel variations in the detector.

[16] http://3dhst.research.yale.edu/Home.html

[17] http://www.ucolick.org/~xavier/IDL/

Table 1
Summary of Near-IR Observations

ID	R.A. (deg)	Decl. (deg)	Mask	Observed Lines
GOODS-S-7892	53.17194	−27.75915	···	[O III], Hα
GOODS-S-43693	53.07129	−27.70580	···	Hα
GOODS-S-43928	53.05158	−27.70476	···	[O III]
UDS-6195	34.42648	−5.25577	···	[O III], Hα
UDS-6377	34.42857	−5.25532	···	[O III], Hα
UDS-7665	34.39076	−5.25080	C	[O III][a]
UDS-10138	34.42336	−5.24226	C	[O III][a]
UDS-12435	34.41087	−5.23481	C	Hα[a]
UDS-12539	34.47389	−5.23423	···	[O III], Hα
UDS-12920	34.39870	−5.23320	C	···
UDS-15319	34.40516	−5.22493	C	···
UDS-19167	34.43140	−5.21212	C	[O III]
UDS-24154	34.39137	−5.19531	C	[O III], Hα
COSMOS-8509	150.09837	2.26596	B	···
COSMOS-8700	150.09740	2.26848	B	···
COSMOS-10599	150.09535	2.28725	B	[O III]
COSMOS-11530	150.11931	2.29688	B	···
COSMOS-12102	150.09728	2.30252	B	[O III], Hα
COSMOS-13184	150.12424	2.31367	B	[O III]
COSMOS-14249	150.11011	2.32459	B	···
COSMOS-14435	150.16232	2.32602	D	···
COSMOS-15091	150.15955	2.33330	D	[O III]
COSMOS-16152	150.18762	2.34469	A	···
COSMOS-16286	150.17699	2.34539	D	[O III][b]
COSMOS-16566	150.17067	2.34830	D	[O III], Hα
COSMOS-17118	150.15114	2.35410	D	[O III]
COSMOS-17162	150.15134	2.35482	A	···
COSMOS-17295	150.18318	2.35537	D	···
COSMOS-17539	150.12814	2.35810	A	···
COSMOS-17839	150.15677	2.36080	A	[O III]
COSMOS-18299	150.17098	2.36536	A	···
COSMOS-18358	150.16719	2.36689	A	[O III]
COSMOS-18582	150.13281	2.36878	A	···
COSMOS-18777	150.18628	2.37054	A	···
COSMOS-19049	150.13886	2.37340	A	[O III][b], Hα
COSMOS-19077	150.18309	2.37295	A	[O III]
COSMOS-20589	150.18056	2.38822	D	···

Notes. All IDs refer to the CANDELS catalog for that particular field. Mask A was observed on 2012 April 21, mask B on 2012 April 22, mask C on 2012 October 10 and 11, and mask D on 2013 March 12, all at the LBT; *GOODS-S-7892* was observed on 2012 December 15, *GOODS-S-43693* on 2012 October 1, *GOODS-S-43928* on 2012 October 15, *UDS-6195* and *UDS-6377* on 2012 August 27, and *UDS-12539* on 2012 August 2 and 27 (120 minutes in the NIR), all at the VLT. Line detections are at least 1σ.

[a] Due to technical problems during the first night of observations, the total exposure time used for these line extractions is only 3600 s in *H*.

[b] Only the [O III] λ5007 component.

Since our objects of interest have virtually no visible continuum, one-dimensional spectral extraction must be done carefully. We must visually search for the lines in the stacked reduced spectra. Since we know the wavelengths of the brightest lines from the grism data, this exercise is straightforward. We isolate the line region according to a S/N cut, and then collapse that region in the wavelength direction to create a slice containing the spatial line profile. This profile is fit with a standard Gaussian function. The width of the distribution, σ, and the center, μ, are then used in the full spectral extraction: a Gaussian function with these same σ and μ values is fit for each pixel row in the spatial direction tracing a constant distance from the edge of the (curved) slit with the amplitude as the only free parameter, reflecting the electron counts at that particular wavelength. All sets of observations were reduced and analyzed separately and the resolution is incorporated into the calculation of the intrinsic line widths to remove systematics in the velocity dispersion measurements. Flux calibration is done by comparing the integrated counts from the LUCI1 spectrum to the integrated line flux from the 3D-HST grism spectrum when possible.

2.3. VLT/X-Shooter Spectroscopy

For an additional six sources, we obtained near-IR and visible spectra using the X-Shooter spectrograph (Vernet et al. 2011) on the 8.2 m ESO Very Large Telescope (VLT). We observed five of the objects initially found in van der Wel et al. (2011): three with previous grism-spectroscopic confirmation in Straughn et al. (2011) and B. Weiner et al. (in preparation), and the two remaining candidates with the largest photometrically inferred line fluxes. A sixth candidate was selected from the Straughn et al. (2011) sample. Observations were done in long-slit mode from 2012 August to December with 40 minute integrations using 1″/0.″9/0.″9 (UVB/VIS/NIR) slits and the 100k/1pt/hg/ 1 × 2 readout mode. See Table 1 for the targets and observing dates. The proximity of objects *UDS-6377* and *UDS-6195* allowed for them to be observed in the same slit.

Although the X-Shooter spectrograph also observes in the UV-Blue, four of our six objects were not observed during dark time, rendering the data unusable. The near-IR region of X-Shooter spans the combined *YJHK* region from 1024–2048 nm, while the visible region spans 559.5–1024 nm. Reduction of the X-Shooter data is performed using version 2.0.0 of the ESO XSHOOTER pipeline,[18] which provides merged, 2D near-IR and visible spectra. Extraction is performed in a similar manner to the LUCI1 data.

3. DYNAMICAL AND STELLAR MASSES

In order to confirm our hypothesis that these systems represent starbursting dwarf galaxies, we must confirm their low stellar masses, low metallicities, and high SFRs. Stellar masses can be constrained through SED fits to broadband photometry, and metallicities can be constrained by observing emission-line ratios, such as [O III]/Hβ. Any SFR is contingent on the nature of the emission lines, since AGNs can also produce very high excitations.

3.1. Methods and Results

In our near-IR spectra, the most prominent lines seen are [O III] λ5007 and Hα, along with their associated complexes ([O III] λ4959+Hβ, and [N II] λλ6548,6584, respectively). With the exception of *COSMOS-12102*, the emission lines can be well fit by a Gaussian function, as described in Maseda et al. (2013). *COSMOS-12102* has the broadest emission lines of the sample. In addition to their broadness, they display some degree of asymmetry and are thus not well fit by Gaussian functions. The skewness could be caused by several processes, such as the presence of strong outflows. Such interpretations are beyond the scope of this paper and demand additional observations.

The best-fitting redshifts, velocity dispersions, and line ratios are given in Table 2.

As described in Maseda et al. (2013), velocity dispersions of the strong emission lines can be used to estimate the

[18] http://www.eso.org/sci/software/pipelines/xshooter/xsh-pipe-recipes.html

Table 2
Sample of Emission Line Galaxies

ID	m_{F140W} (AB)	r_{eff}[a] (kpc)	$f_{H\alpha}$	$EW_{H\alpha}$ (Å)	$f_{[O\,III]}$	$EW_{[O\,III],5007}$ (Å)	z_{spec}	$\sigma_{H\alpha}$ (km s^{-1})	$\sigma_{[O\,III]}$ (km s^{-1})
GOODS-S-33131	23.66 ± 0.08	0.68 ± 0.62	...	...	7.36 ± 2.99	693 ± 47	1.687	48.7 ± 4.3	52.3 ± 5.7
GOODS-S-43693	24.36 ± 0.12	0.35 ± 0.06	...	...	16.9 ± 0.88	861 ± 66	1.738	54.4 ± 4.5	...
GOODS-S-43928	24.59 ± 0.15	1.9 ± 0.48	4.5 ± 1.2[b]	199[b]	3.7 ± 1.6[b]	176[b]	1.472	...	31.4 ± 8.2
UDS-6195	24.26 ± 0.13	1.4 ± 0.42	...	...	...	701 ± 95[c]	1.687	69.9 ± 4.9	54.7 ± 6.1
UDS-6377	24.53 ± 0.17	0.67 ± 0.04	...	...	...	731 ± 86[c]	1.664	54.5 ± 4.5	48.2 ± 5.9
UDS-7665	25.40 ± 0.14	0.51 ± 0.08	...	...	13.7 ± 2.76	803 ± 162	2.298	...	57.8 ± 9.7
UDS-10138	23.77 ± 0.03	0.75 ± 0.08	...	...	10.9 ± 0.57	322 ± 17	2.151	...	80.9 ± 10.0
UDS-12435	23.42 ± 0.03	1.0 ± 0.06	...	...	12.2 ± 0.94	263 ± 31	1.611	65.2 ± 11.3	...
UDS-12539	23.39 ± 0.06	1.3 ± 0.07	...	...	35.5 ± 2.73	713 ± 42	1.621	81.3 ± 4.3	71.1 ± 5.7
UDS-19167	23.99 ± 0.04	1.1 ± 0.20	...	...	21.5 ± 2.82	723 ± 95	2.185	...	54.2 ± 9.4
UDS-24154	23.78 ± 0.04	1.8 ± 0.16	...	...	21.9 ± 3.09	503 ± 34	2.297	72.5 ± 13.1	61.0 ± 10.8
COSMOS-10599	24.47 ± 0.26	0.67 ± 0.16	...	...	11.8 ± 0.89	714 ± 85	2.220	...	30.9 ± 9.0
COSMOS-12102	22.82 ± 0.06	1.6 ± 0.08	19.9 ± 1.0	360 ± 18	49.4 ± 2.28	630 ± 29	1.463	230.8 ± 14.7	241.3 ± 12.7
COSMOS-13184	23.91 ± 0.16	0.53 ± 0.10	...	...	11.5 ± 2.94	598 ± 189	2.199	...	40.3 ± 8.9
COSMOS-15091	25.46 ± 0.13	0.75 ± 0.11	...	...	5.99 ± 3.61	628 ± 152	1.583	...	38.2 ± 10.0
COSMOS-16286	24.64 ± 0.11	1.1 ± 0.13	0.39 ± 3.32	41 ± 345	8.76 ± 3.46	888 ± 351	1.444	...	46.7 ± 14.4
COSMOS-16566	24.60 ± 0.09	1.4 ± 0.09	4.22 ± 3.26	560 ± 432	7.28 ± 3.58	388 ± 191	1.437	25.5 ± 14.0	32.8 ± 8.4
COSMOS-17118	24.16 ± 0.13	4.8 ± 0.33	...	...	12.3 ± 4.22	493 ± 169	1.656	...	46.5 ± 8.8
COSMOS-17839	24.36 ± 0.24	0.99 ± 0.06	3.27 ± 3.20	325 ± 230	16.3 ± 3.58	1126 ± 247	1.412	...	43.3 ± 8.9
COSMOS-18358	22.84 ± 0.04	1.6 ± 0.02	...	...	30.2 ± 0.97	316 ± 26	1.645	...	55.9 ± 9.0
COSMOS-19049	22.93 ± 0.05	2.3 ± 0.06	16.4 ± 1.2	368 ± 28	20.9 ± 2.20	330 ± 35	1.370	81.9 ± 50.2	122.0 ± 11.0
COSMOS-19077	23.69 ± 0.12	1.6 ± 0.05	...	...	20.5 ± 0.77	536 ± 20	1.649	...	47.7 ± 9.5

Notes. All fluxes are given in units of 10^{-17} erg s^{-1} cm^{-2}. Equivalent widths are quoted in the restframe. A description of the size measurements is given in Section 3.1.
[a] van der Wel et al. (2012).
[b] Straughn et al. (2011).
[c] van der Wel et al. (2011).

dynamical masses, assuming the line width comes entirely from gravitational motion in a virialized system such that

$$M_{dyn} = 3\frac{r_{eff}\sigma^2}{G}. \quad (1)$$

Here, σ is the observed line width from our NIR spectrum and r_{eff} is the effective radius of the galaxy from the public CANDELS catalog released in van der Wel et al. (2012). Typical objects are 1.0 ± 0.1 kpc in both the J_{F125W}- and H_{F160W}-bands.

These dynamical masses are listed in Table 3, ranging from $10^{8.39}$ to $10^{10.6}$ $M_\odot$, with a median mass of $10^{9.13}$ $M_\odot$. The uncertainty in the dynamical mass estimate comes primarily from the systematic uncertainty in the proportionality constant of 3, which relates the intrinsic velocity v to the observed velocity dispersion σ, which we assume to be the same factor of 33% as Rix et al. (1997), since in most cases our observed line widths and physical sizes are well-constrained. Further details can be found in Maseda et al. (2013). Amorín et al. (2012), in a study of "green peas," observe multiple star-forming regions and gas flows, which are seen as asymmetries and broad, low-intensity wings. While we do not see such clear evidence for outflows via asymmetric line profiles (*COSMOS-12102* excepted) or broad wings, we cannot currently rule out contributions of non-gravitational motions to the observed line widths since we only detect the bright, central line regions, and not a second component in the form of low surface brightness features that would indicate the presence of outflows. As such, the contribution of outflows to the width of the detected high surface brightness features is unconstrained and the true dynamical mass may be lower than prescribed by Equation (1).

Multi-band photometry is obtained from 3D-HST (Skelton et al. 2014), covering 0.3–24 μm for the GOODS-S (23 bands), UDS (17 bands), and COSMOS (31 bands) fields. Visual inspection of the *Spitzer/IRAC* frames show contamination from nearby objects in *UDS-7665*, *COSMOS-13184*, and *COSMOS-15091*, so their SEDs do not include the contaminated points. For the same reason, we do not include any the data from the 5.8 and 8 μm IRAC channels for this sample, even though it is available as part of the publicly released catalogs. Only three objects have detections at 24 μm with *Spitzer/MIPS* (the photometric measurements use a deblending technique is described in Fumagalli et al. 2013), and an upper limit of 10 μJy is adopted for the remainder of the sample.

We fit the broadband SEDs of our galaxies in the same manner as Maseda et al. (2013) using a custom version of the MAGPHYS code[19] (da Cunha et al. 2008), which computes the emission by stellar populations and the attenuation by dust in a two-component ISM, and includes nebular line emission computed self-consistently using the Pacifici et al. (2012) model (Charlot & Longhetti 2001; Pacifici et al. 2014). The broad-band fluxes computed with this model include the contamination by emission lines, so they can be directly and robustly compared with the observed fluxes that we know are likely emission-line contaminated for these galaxies (at these and higher redshifts, it has been shown that an improper treatment of nebular contamination to broadband magnitudes results in an overestimate of stellar masses and hence an underestimate in sSFRs, e.g., Atek et al. 2011; Curtis-Lake et al. 2013; Stark et al. 2013). MAGPHYS compares the input photometry to an extensive library of SED templates spanning a wide range in parameters such as star formation history, metallicity, age, and dust optical depth using a Bayesian method. As such, all results

[19] http://www.iap.fr/magphys

Table 3
Derived Parameters

ID	log $M_{\rm dyn}$ ($M_\odot$)	log $M_\star$ ($M_\odot$)	log Age (yr)	Z ($Z_\odot$)	log SFR ($M_\odot$ yr^{-1})	τ_V
GOODS-S-33131	9.05 ± 0.30	$8.91^{+0.050}_{-0.075}$	$7.78^{+0.190}_{-0.065}$	$0.321^{+0.180}_{-0.132}$	$0.892^{+0.030}_{-0.080}$	$0.242^{+0.030}_{-0.085}$
GOODS-S-43693	8.86 ± 0.31	$8.28^{+0.195}_{-0.050}$	$7.50^{+0.240}_{-0.045}$	$0.147^{+0.160}_{-0.098}$	$0.557^{+0.090}_{-0.065}$	$0.137^{+0.050}_{-0.090}$
GOODS-S-43928	9.12 ± 0.38	$8.83^{+0.070}_{-0.065}$	$8.39^{+0.175}_{-0.260}$	$0.169^{+0.272}_{-0.120}$	$0.262^{+0.190}_{-0.080}$	$0.327^{+0.505}_{-0.145}$
UDS-6195	9.47 ± 0.33	$7.60^{+0.320}_{-0.300}$	$6.85^{+0.385}_{-0.300}$	$0.299^{+0.300}_{-0.130}$	$0.447^{+0.300}_{-0.065}$	$0.027^{+0.085}_{-0.300}$
UDS-6377	9.04 ± 0.31	$8.32^{+0.140}_{-0.300}$	$6.96^{+0.735}_{-0.300}$	$0.081^{+0.096}_{-0.022}$	$1.08^{+0.300}_{-0.580}$	$1.12^{+0.025}_{-0.835}$
UDS-7665	9.07 ± 0.33	$8.52^{+0.300}_{-0.300}$	$7.04^{+0.300}_{-0.300}$	$0.155^{+0.300}_{-0.300}$	$1.21^{+0.300}_{-0.300}$	$0.862^{+0.300}_{-0.300}$
UDS-10138	9.53 ± 0.31	$8.43^{+0.270}_{-0.300}$	$7.10^{+0.430}_{-0.300}$	$0.177^{+0.010}_{-0.300}$	$1.05^{+0.300}_{-0.135}$	$0.112^{+0.300}_{-0.040}$
UDS-12435	9.47 ± 0.33	$9.42^{+0.045}_{-0.055}$	$8.60^{+0.050}_{-0.130}$	$0.189^{+0.392}_{-0.138}$	$0.677^{+0.070}_{-0.030}$	$0.082^{+0.085}_{-0.040}$
UDS-12539	9.66 ± 0.30	$8.67^{+0.300}_{-0.300}$	$7.05^{+0.300}_{-0.300}$	$0.581^{+0.300}_{-0.300}$	$1.29^{+0.300}_{-0.300}$	$0.667^{+0.300}_{-0.300}$
UDS-19167	9.35 ± 0.34	$8.96^{+0.300}_{-0.300}$	$8.58^{+0.300}_{-0.300}$	$0.085^{+0.300}_{-0.300}$	$1.02^{+0.300}_{-0.300}$	$0.192^{+0.300}_{-0.300}$
UDS-24154	9.67 ± 0.33	$9.10^{+0.100}_{-0.300}$	$7.49^{+0.165}_{-0.300}$	$0.531^{+0.300}_{-0.030}$	$1.38^{+0.300}_{-0.050}$	$0.462^{+0.105}_{-0.005}$
COSMOS-10599	8.65 ± 0.40	$8.72^{+0.240}_{-0.300}$	$7.49^{+0.245}_{-0.300}$	$0.531^{+0.300}_{-0.362}$	$1.00^{+0.015}_{-0.020}$	$0.462^{+0.080}_{-0.300}$
COSMOS-12102	10.8 ± 0.30	$9.57^{+0.300}_{-0.300}$	$8.40^{+0.300}_{-0.300}$	$0.155^{+0.300}_{-0.300}$	$1.63^{+0.300}_{-0.300}$	$1.77^{+0.300}_{-0.300}$
COSMOS-13184	8.78 ± 0.36	$9.00^{+0.070}_{-0.220}$	$7.28^{+0.365}_{-0.095}$	$0.087^{+0.068}_{-0.040}$	$1.29^{+0.230}_{-0.120}$	$0.407^{+0.245}_{-0.110}$
COSMOS-15091	8.88 ± 0.37	$7.92^{+0.280}_{-0.120}$	$7.61^{+0.965}_{-0.105}$	$0.169^{+0.042}_{-0.084}$	$0.062^{+0.200}_{-0.020}$	$0.077^{+0.115}_{-0.300}$
COSMOS-16286	9.22 ± 0.40	$8.44^{+0.160}_{-0.125}$	$7.92^{+0.525}_{-0.650}$	$0.171^{+0.044}_{-0.054}$	$0.317^{+0.440}_{-0.325}$	$1.05^{+0.500}_{-0.850}$
COSMOS-16566	9.02 ± 0.37	$8.60^{+0.040}_{-0.045}$	$8.29^{+0.065}_{-0.110}$	$0.137^{+0.324}_{-0.074}$	$0.147^{+0.035}_{-0.045}$	$0.037^{+0.050}_{-0.020}$
COSMOS-17118	9.86 ± 0.33	$8.47^{+0.210}_{-0.315}$	$7.66^{+0.920}_{-0.425}$	$0.155^{+0.136}_{-0.070}$	$0.752^{+0.300}_{-0.085}$	$0.192^{+0.105}_{-0.010}$
COSMOS-17839	9.11 ± 0.34	$8.19^{+0.135}_{-0.190}$	$7.43^{+0.335}_{-0.195}$	$0.091^{+0.300}_{-0.018}$	$0.392^{+0.105}_{-0.035}$	$0.037^{+0.005}_{-0.300}$
COSMOS-18358	9.54 ± 0.32	$9.43^{+0.300}_{-0.300}$	$8.12^{+0.300}_{-0.300}$	$0.629^{+0.300}_{-0.300}$	$1.11^{+0.300}_{-0.300}$	$0.037^{+0.300}_{-0.300}$
COSMOS-19049	10.4 ± 0.30	$9.85^{+0.168}_{-0.300}$	$8.36^{+0.165}_{-0.300}$	$0.081^{+0.046}_{-0.300}$	$1.31^{+0.120}_{-0.300}$	$1.72^{+0.200}_{-0.300}$
COSMOS-19077	9.40 ± 0.34	$8.92^{+0.300}_{-0.225}$	$8.05^{+0.300}_{-0.555}$	$0.173^{+0.358}_{-0.300}$	$0.692^{+0.285}_{-0.300}$	$0.197^{+0.265}_{-0.300}$

Notes. Quoted values for $M_\star$, age (mass-weighted), Z, SFR, and τ_V are the medians of the probability distributions from MAGPHYS with associated +/– 1σ values. Cases where we have an uncertainty of 0 occur when the data cannot be well explained by the models and not when the models constrain the output parameters well, which manifests itself as a large χ^2 value. As such, we will adopt an uncertainty of 0.3 dex (the typical uncertainty for stellar masses obtained from fitting broadband photometry, Conroy 2013) in those cases to be used in the subsequent analysis.

quoted are the medians of the posterior probability distributions for each parameter marginalized over the other parameters, with uncertainties corresponding to the 16th and 84th percentiles for the distribution. In cases where the output probabilities are not well constrained, typically due to the (potentially systematic) uncertainties in the photometry, we adopt an uncertainty of 0.3 dex in the relevant parameter: a formal error of 0 is indicative of the models not fitting the data well. 0.3 dex is the typical uncertainty in determining stellar masses from fits to broadband photometry (Conroy 2013). An example probability distribution for some of the various parameters is shown in Figure 2. Results of the SED fitting are given in Table 3, showing high sSFRs, low stellar masses, low metallicities, young ages, and low dust extinction. Since the NIR sizes represent the restframe optical and hence the stellar continuum at these redshifts, we are probing the same physical region in both mass estimates.

The median τ_V (V-band optical depth seen by young stars in the birth clouds) is 0.2, consistent with the very blue observed SEDs. Even with the lack of infrared data to directly probe the dust content of these systems, we can place a limit on the dust mass based on the total dust attenuation and luminosity inferred from the SED fits and a prior on the dust temperature as in da Cunha et al. (2013). Resulting limits are $\lesssim 10^7$ $M_\odot$ and hence negligible compared to the stellar masses.

As mentioned above, the critical piece of additional information that we include to perform these fits is the line fluxes. We see a median SFR of ~ 9 $M_\odot$ yr^{-1}, which, combined with the low stellar masses, justifies our emission line criteria for the selection of starbursts. By separating the emission lines from the stellar continuum light, we are better able to trace the gas-phase metallicities. This results in metallicity estimates consistent with direct probes of the oxygen abundance using emission-line ratios (see Section 4.2). In addition, it allows for better estimates of the extinction in the H II regions, which produce the aforementioned τ_V values.

Our model library of stellar population SEDs contains a broad range of complex star formation histories (SFHs), including bursts on top of extended SFHs with a variety of evolutionary trends (rising, falling, and constant). Despite these efforts, which far exceed the still common use of exclusively exponentially declining SFHs, systematic uncertainties remain. In particular for galaxies with significant star formation activity in the past $\sim$50 Myr, as is the case here, red supergiants with individual luminosities of $\sim 10^5$ $L_\odot$ can easily outshine more massive populations of stars with any age $>$50 Myr, especially in the near-infrared. Prior knowledge of the SFH is needed to address this issue, producing a degree of circularity in the problem of stellar mass determinations. Keeping this in mind, we proceed and note where necessary that for galaxies with estimated ages $\lesssim$50 Myr the mass (and age) estimates must be lower limits, as seen in tails to higher masses and mass-weighted ages, e.g., Figure 2.

Extracted near-IR spectra and SED fitting results for *GOODS-S-33131* are shown in Figure 3(a); all remaining objects in our sample are shown in Figures 3(b), (c), and 4. Telluric corrections are applied as needed.

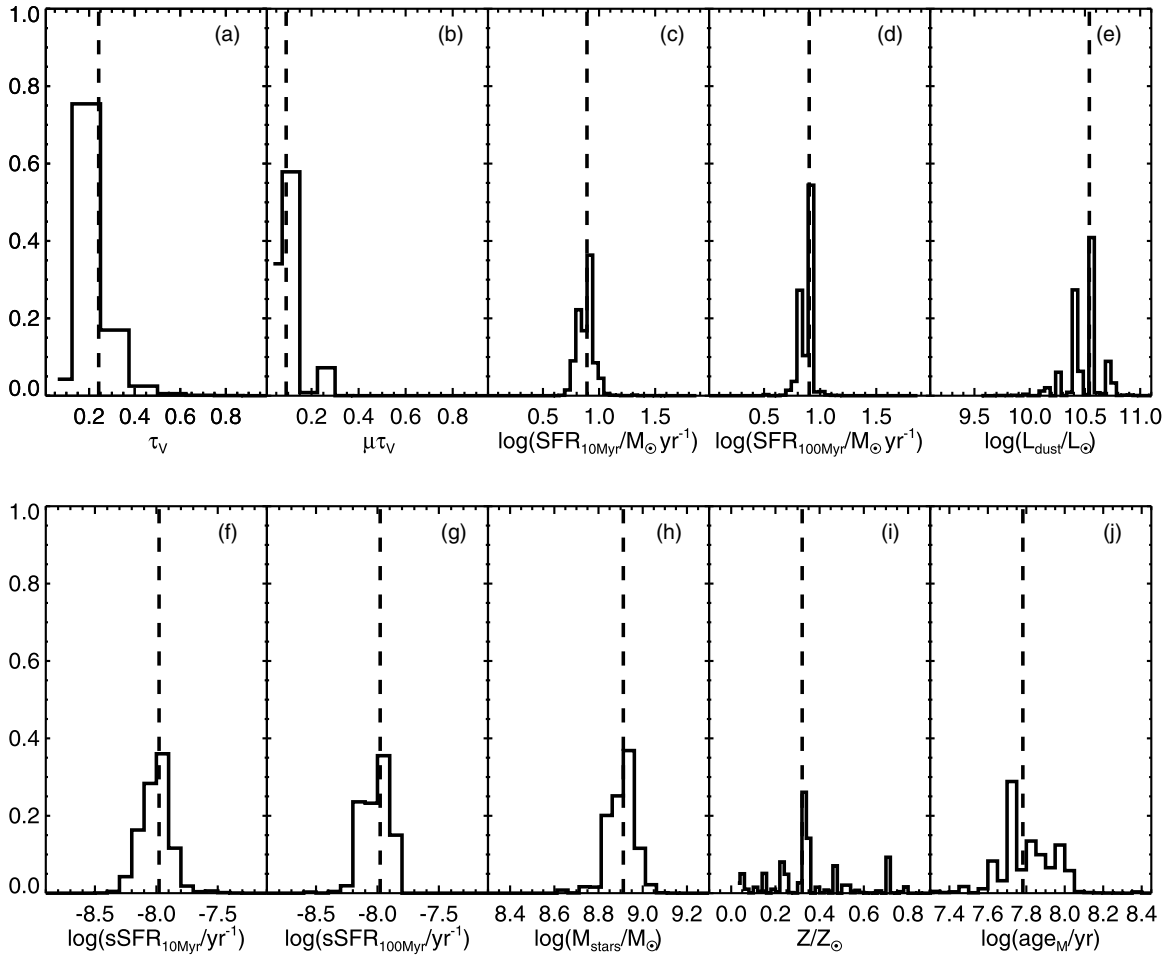

Figure 2. Probability distributions from MAGPHYS for *GOODS-S-33131*. Vertical dashed lines denote the medians of the output probability distribution, which are quoted throughout this work. Panels denote the following: (a) *V*-band optical depth seen by young stars in the birth clouds; (b) *V*-band optical depth seen by stars in the diffuse ISM; (c) star formation rate averaged over the last 10 Myr; (d) total dust luminosity; (e) star formation rate averaged over the last 10 Myr divided by stellar mass; (f) stellar mass; (g) stellar metallicity (which we set equal to the gas-phase metallicity); and (h) mass-weighted age.

As demonstrated in Maseda et al. (2013), there is a tight, linear relation between the total dynamical and stellar mass estimates. Figure 5 may show that the stellar-to-dynamical mass ratio correlates with the (mass-weighted) age as well. This qualitatively agrees with the model in which a non-replenished reservoir of gas is turned into stars, such that the older systems have formed a proportionally larger number of stars. For further discussion, see Section 5. To date, these systems represent the lowest dynamical masses ever measured at this epoch, and typically have lower stellar masses than those galaxies in similar star-forming spectroscopic surveys (e.g., Masters et al. 2014; see also Figure 6 and Section 3.2). Note that the systematic errors in $M_{\rm dyn}$ dominate the size of the error bar. *COSMOS-12102* shows a broad and asymmetric line profile for which the line width most likely does not trace the underlying gravitational potential. The lack of a clear trend in the relationship between the two main "observed" quantities, $M_\star$ and σ, can be seen in Figure 7, which suggests that any relationship between $M_\star$ and $M_{\rm dyn}$ must be driven by a relationship between the size of the galaxy and $M_\star$. Figure 8 shows this relationship, as our sample lies on or below the observed size–mass relation for late-type galaxies at $2 < z < 2.25$ as found in van der Wel et al. (2014) in 3D-HST and CANDELS.

The extreme nature of the star-formation in these systems is clearly seen in Figure 9. The stellar masses measured here are beginning to probe the same regime as van der Wel et al. (2011) and Brammer et al. (2012b), with similar sSFR values. Note that the sSFR values obtained from MAGPHYS are averaged over the last 10 Myr: given the ephemeral nature of the bursts, the current (s)SFR may not reflect the most vigorous period of star formation in these systems. These are more than an order of magnitude in excess of the sSFR values characteristic of the star-forming population of massive galaxies at similar redshifts, measured in Hα from Fumagalli et al. (2012).

3.2. Comparison to Other Studies

At lower redshifts $0.11 \leqslant z \leqslant 0.93$, Amorín et al. (2014a, 2014b) have isolated a sample of EELGs selected on [O III] flux that show remarkable similarities to our sample with sizes $r_{1/2} \sim 1.3$ kpc, masses 10^7–10^{10} $M_\odot$, sSFR values 10^{-7}–10^{-9} yr^{-1}, and metallicity estimates of 0.05–0.6 $Z_\odot$ (some determined "directly" using the [O III] λ4363 line as well; see Section 4.2). Deep *HST*/*ACS I*-band images reveal that most (80%) of their EELG sample show non-axisymmetric morphologies indicative of recent mergers or interactions. Only samples that are complete over the redshift ranges in question will allow for a direct comparison between the two populations, which are currently only split artificially according to either

optical or near-IR observations. However, caution must be taken in any interpretation: the much higher number density at $z \sim 1.7$ from van der Wel et al. (2011) than at very low-z from Cardamone et al. (2009) implies that there could be a very different mechanism involved in triggering the bursts. Connecting the two populations in a qualitative sense is the subject of ongoing work.

Our current observations do not allow us to make strong conclusions about the internal dynamics of individual systems. Currently, the only opportunities to study the internal dynamics of such small systems at high-redshift is with gravitational lensing: Jones et al. (2010) note that their $z \sim 2$–3 strongly lensed galaxies would resemble mergers or dispersion-dominated systems without the additional spatial resolution provided by the lensing. Two objects similar to those presented here are *MACS J2135-0102* ($M_\star = 9.8\ M_\odot$, $z = 3$, $r_{1/2} = 1.75$ kpc, SFR = 40 $M_\odot$ yr^{-1}, $\sigma_{\rm H\alpha} = 54$ km s^{-1}, $V_c = 67$ km s^{-1}) from Jones et al. (2010) and *SHIZELS-10* ($M_\star = 9.4\ M_\odot$, $z = 1.45$, $r_{1/2} = 2.3$ kpc, SFR = 10 $M_\odot$ yr^{-1}, $\sigma_{\rm H\alpha} = 64$ km s^{-1}, $V_c = 26$ km s^{-1}) from Swinbank et al. (2012), which both appear to have a (relatively weak) rotational component to their dynamics. Further discussion of the dynamics of our present sample is deferred to Section 5.

Several other studies have begun to characterize the star-forming properties of high-z EELGs using various techniques. The most obvious comparable study to this work is the WFC3 Infrared Spectroscopic Parallels survey (WISP; Atek et al. 2010), and specifically the study of Masters et al. (2014). As a similar WFC3 grism survey, they are also able to select galaxies based on emission lines instead of photometric techniques, and thus can isolate a sample of high-EW ELGs. Masters et al. (2014) present a sample of 26 such ELGs with a median restframe [O III] EW of 154 Å (our median is 629 Å). These galaxies show similarly low velocity dispersions (~70 km s^{-1}) and hence also have dynamical masses $\lesssim 10^{10}\ M_\odot$. They derive stellar masses using an assumed M/L ratio and star-formation history in a similar fashion to van der Wel et al. (2011), which have been shown to generally agree with SED-derived stellar masses (Maseda et al. 2013), and have also begun to probe the $M_\star \lesssim 10^9\ M_\odot$ regime. Specific discussion of their metallicity estimates is deferred to Section 4.2.

In addition to WISP, narrowband studies have also begun to uncover the general star-forming population of galaxies at $z > 1$, probing stellar masses below $10^{9.5}\ M_\odot$. Sobral et al. (2014) use data from the HiZELS survey to study Hα emitters at redshifts $z = 0.84$, 1.47, and 2.23. The size of their survey area (~2 deg^2) and the depth of the imaging allows them to isolate large and pure samples of Hα emitters down to a restframe Hα+[N II] EW of 25 Å, constraining the stellar mass function of star-forming galaxies down to $10^{9.5}\ M_\odot$ at these redshifts. Indeed, their sample also includes a number of objects with restframe Hα+[N II] EW values in excess of 300 Å and with stellar masses from SED-fitting below $10^9\ M_\odot$. Their results for the characteristic sSFR (i.e., the typical SFR for a galaxy at a given mass and redshift divided by its mass) as a function of mass and redshift is shown in Figure 9. While some of our objects can be considered "normal" at these redshifts according to this determination, a majority of them still have higher sSFRs than expected, albeit typically within 1 dex. This reinforces the notion that these objects are the high-EW tail of the total distribution of star-forming galaxies at these redshifts and do not comprise a genuinely separate population (van der Wel et al. 2011).

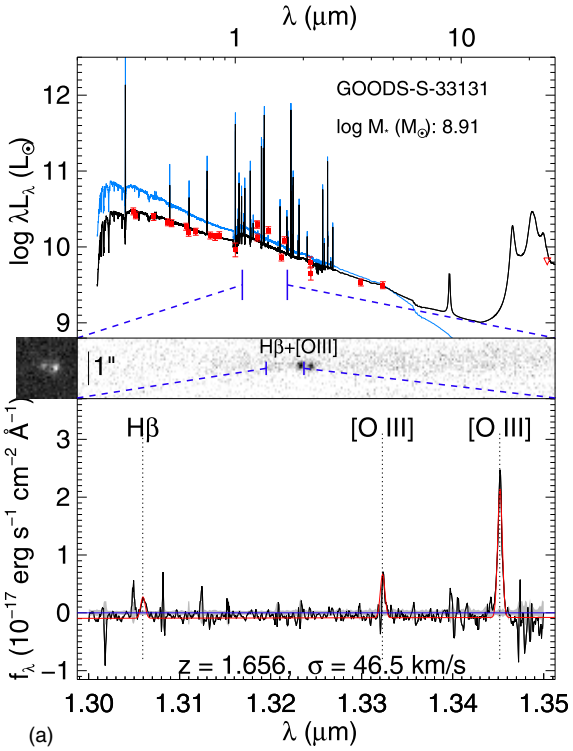

Figure 3. (a) Example of a broadband SED including best-fitting model (top), WFC3 grism image/spectrum (middle), and X-Shooter spectrum (bottom) for an object in our sample. The NIR spectra for the remaining objects can be seen in panels (b) for [O III] and (c) for Hα; the SEDs for the remaining objects can be seen in Figure 4. SED fits are performed as described in Section 3.1, with red points denoting the measured photometry (open points are upper limits), the blue curve denoting the non-attenuated SED, and the black curve denoting the observed SED including dust attenuation. The direct F140W image is shown on the left and the dispersed G141 grism image is shown on the right, with important spectral lines labeled and contamination subtracted as described in I. Momcheva et al. (in preparation). The X-Shooter spectrum is smoothed by three pixels and is flux-calibrated according to the grism line flux. The shaded gray area represents the +/−1σ flux uncertainties and the red curve shows the best- fitting model of the emission lines. (b) WFC3 G141 grism and LUCI1 or X-Shooter spectrum. The spectra are smoothed by three pixels and are flux-calibrated according to the grism line fluxes. The shaded gray area represents the +/−1σ flux uncertainties and the red curve shows the best-fitting model of the emission lines. The dotted lines show the position of the [O III] $\lambda\lambda$5007, 4959 and Hβ emission lines. (c) WFC3 G141 grism and LUCI1 or X-Shooter spectrum, same as Figure 3(b) but for the detected Hα lines. The positions of the [N II] lines as well as the Hα line are denoted by the dotted lines.

(A color version of this figure is available in the online journal.)

4. EMISSION-LINE RATIOS

4.1. Starbursts or AGNs?

So far, the main caveat is that we have assumed that star formation is primarily responsible for the strong line emission. The most compelling evidence to support this assumption is the relation between stellar mass and dynamical mass, and that the dynamical masses, with two exceptions, do not exceed $10^{10}\ M_\odot$ (Maseda et al. 2013). Such a result would be entirely coincidental in the case that the emission lines are powered by AGNs since the width of AGN emission lines is not coupled to the stellar mass of the host galaxy. In other words, we observe narrow emission lines in these small (~1 kpc) systems, while typical AGN narrow line regions have much larger emission-line widths $\sigma > 200$ km s^{-1} (Osterbrock & Mathews 1986). However, it is useful to look for evidence of AGN contributions.

Although low-metallicity, low-mass AGNs are exceedingly rare in the local universe (Izotov & Thuan 2008), there is

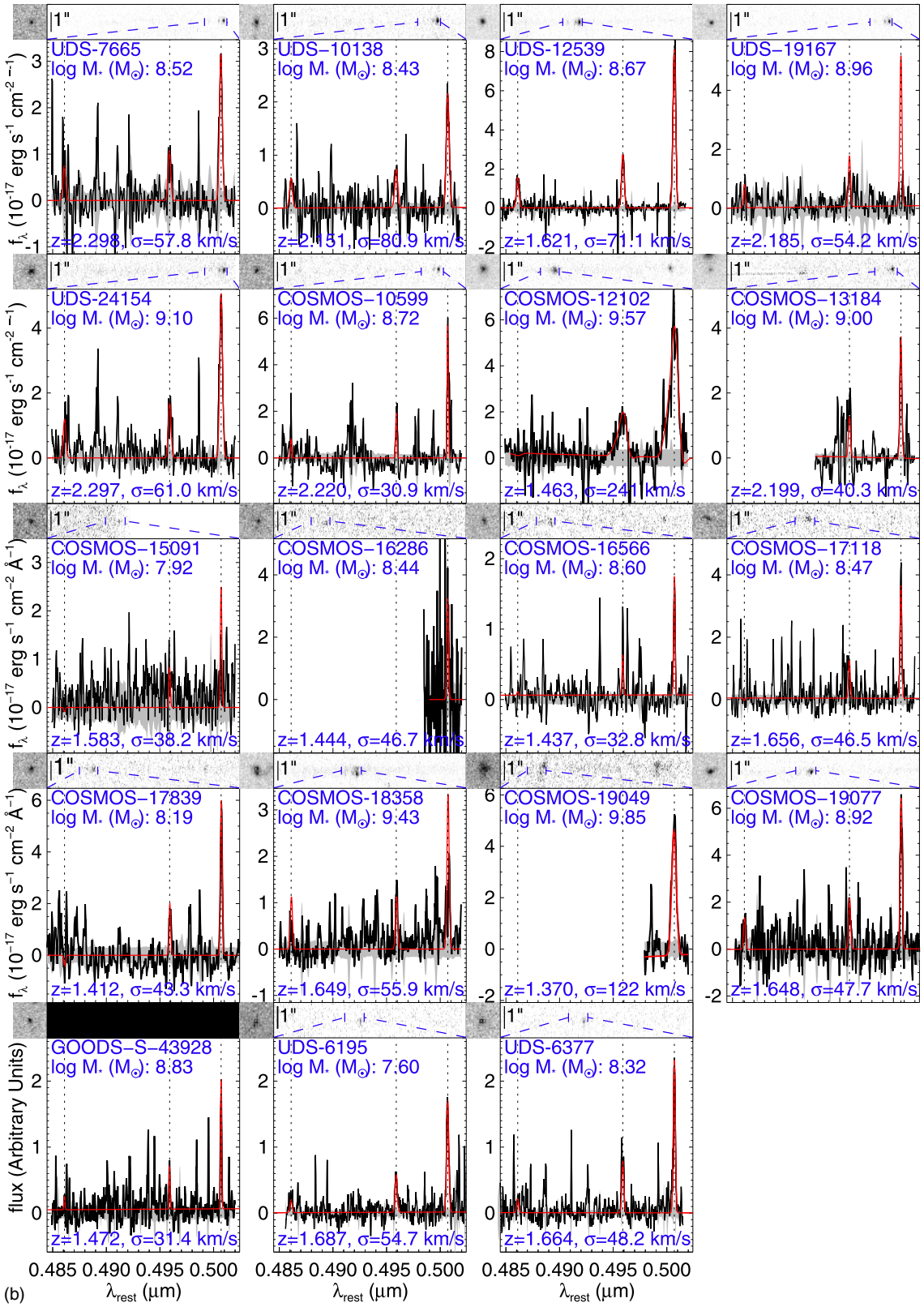

Figure 3. (Continued)

some evidence that they may be more common at higher-z (Trump et al. 2011; Xue et al. 2012; Reines et al. 2013). Such AGNs could cause large observed line fluxes. At $z > 1$, AGN identification with a simple diagnostic such a high [O III] λ5007/Hβ ratio becomes insufficient by itself, as shown by Trump et al. (2013). We thus utilize the "BPT" diagnostics of Baldwin et al. (1981) for the objects in our sample with measurements of [N II] and/or [S II] in addition to Hα. Given that these lines are typically quite weak in star forming galaxies and the strong influence of OH skylines in our NIR spectra, in some instances

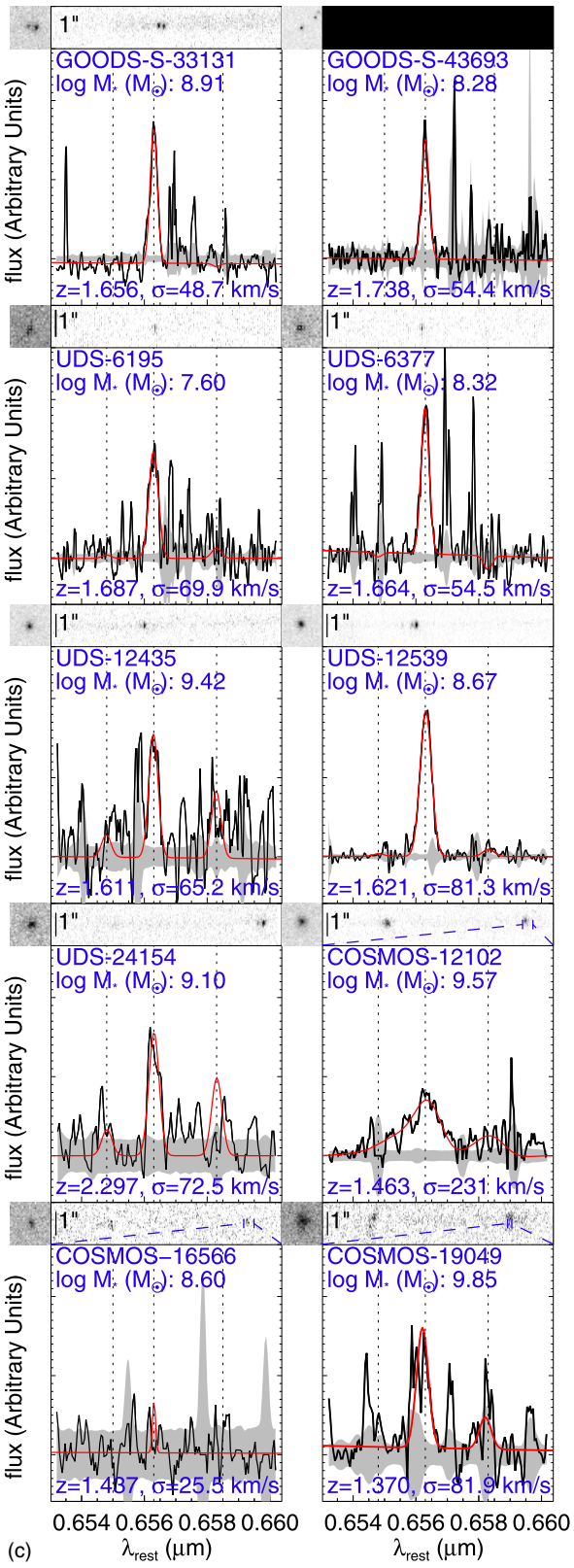

Figure 3. (Continued)

we can only place an upper limit on the ratios of those lines with Hα. These two BPT diagrams are shown in the left and central panels of Figure 10 with contours showing galaxies from the SDSS MPA-JHU value-added DR7 catalog.

Most of our points plausibly lie on an extension of the star-forming region of the BPT diagrams and not on the extension of the AGN region, or at least they lie far from the main locus of AGN-powered emission lines. However, low-metallicity AGNs can lie in the star-forming region as well (Groves et al. 2006; Kewley et al. 2013), preventing us from completely ruling out the contribution of AGNs to our sample with these diagnostics. In some cases we observe higher [O III]/Hβ ratios compared to the other star-forming galaxies, but this can be explained simply by higher ionizations and lower metallicities in these systems compared to the low-z sample of SDSS galaxies. Kewley et al. (2013) find that star-forming galaxies at $z > 1$ are consistent with models that have more extreme ISM conditions than those in the local universe.[20] High electron temperatures (discussed in the next section) support such a hypothesis. This would be a further, unexplained coincidence if they are AGNs in addition to the low dynamical masses described previously. While Trump et al. (2011) suggest that AGNs are widespread in low-mass $1.3 < z < 2.4$ galaxies, the emission lines are not actually dominated by AGNs. This is most evident in the $L_{0.5-10\,\mathrm{keV}}/L_{[\mathrm{O\,III}]}$ relationship: the [O III] lines have some AGN contribution, but (on average) less than 50%.

Additionally, we utilize the Mass-Excitation (MEx) diagnostic of Juneau et al. (2011), which combines the [O III] λ5007/Hβ ratio with the stellar mass. Trump et al. (2013) conclude that this diagnostic also gives a meaningful probabilistic constraint on the AGN/SF nature of galaxies at $z > 1$ using a combination of the BPT diagnostics and X-ray data. While this diagnostic is easily applicable to our data, we can not constrain the MEx AGN/star-forming probabilities for most of our sample given that it is not properly calibrated for objects with such low metallicities and high sSFRs, AGNs or otherwise: the five objects with a probability of star formation (P_{SF}, compared to the probability that they are AGNs; *COSMOS-18358*, *COSMOS-13184*, *COSMOS-10599*, *UDS-24154*, and *UDS-12435*) have a median P_{SF} value of 0.940, firmly placing them in the star-forming regime. The remaining objects, while probabilistically unconstrained, still lie far from the population of AGNs in the MEx diagnostic plot, as shown in Figure 10.

We can place other constraints on the AGN nature of these systems in much the same way as van der Wel et al. (2011), i.e., independent of any measured emission line ratio(s). Most objects in our sample do not have strong 24 μm detections using *Spitzer*/*MIPS*: *COSMOS-18358* has a MIPS 24 μm flux of 21.5 $\pm$ 9.0 μJy and clearly appears to be a merger; *COSMOS-19049* has a flux of 14.1 $\pm$ 8.6 μJy, is physically large with $r_{\mathrm{eff}} = 2.3$ kpc, and also has broad lines with $\sigma_{[\mathrm{O\,III}]} = 122\ \mathrm{km\,s^{-1}}$; *COSMOS-12102* has a flux of 55.3 $\pm$ 8.7 μJy and is further discussed below. While none of our objects have X-ray detections, GOODS-S is also the only field with sufficient depth to find $z \sim 2$ AGNs which are not quasars. That being said, it is possible to hide even a rapidly accreting X-ray AGNs in a low mass galaxy (Aird et al. 2012). The consistent (and resolved) J_{F125W}- and H_{F160W}-sizes, as well as the sizes of the emission lines in the grism spectra, rule out the presence of a strong point source dominating the emission.

An exception could be *COSMOS-12102*, illustrated by the star in Figure 10, which is also has the largest line width in our sample. Reines et al. (2013) find active black holes in similar mass dwarf galaxies with broad Hα emission in the local universe with $M_{\mathrm{BH}} \lesssim 10^6\ M_\odot$. Using their relation

[20] While beyond the scope of this paper, we would like to point out the large uncertainties in assumptions about the ISM conditions in galaxies at high redshift given the lack of knowledge about ionizing spectrum of hot stars at these early times and low metallicities.

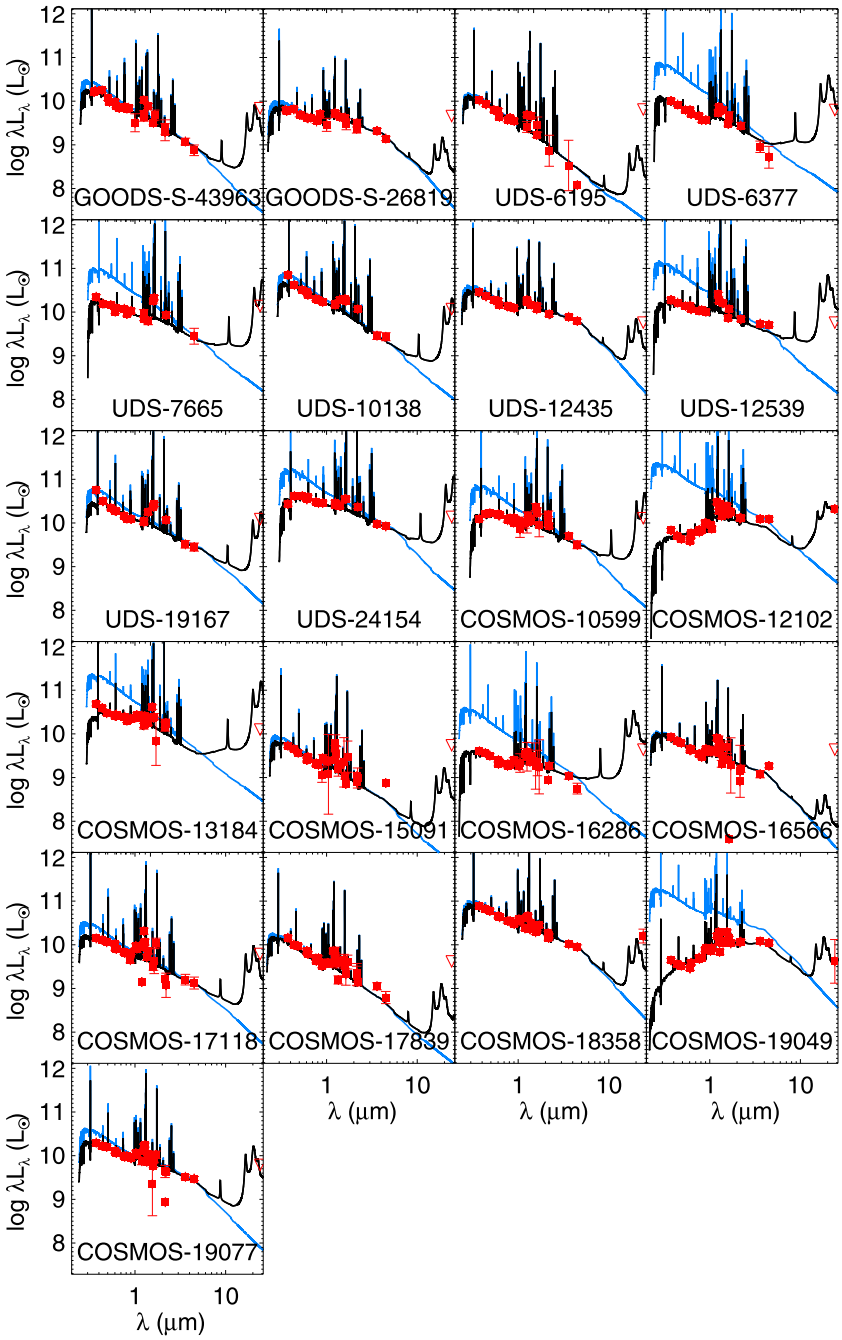

Figure 4. Best-fit SEDs for the remaining objects in the sample. The fits are performed as described in Section 3.1, with red points denoting the measured photometry (open points are upper limits), the blue curve denoting the total non-attenuated SED, and the black curve denoting the observed SED including dust attenuation.
(A color version of this figure is available in the online journal.)

(Equation (5)) of $L_{H\alpha}$ and $FWHM_{H\alpha}$ to M_{BH}, *COSMOS-12102* has a black hole mass of $\sim 10^{6.2}$ $M_{\odot}$, which is in their observed range. The mass determination is fraught with systematic uncertainties, such as variations in the geometry of the broad-line region and that at least some of the Hα luminosity comes from star formation, but we cannot conclusively rule out some AGN contribution for this galaxy.

4.2. Metallicity

In order to measure the gas-phase oxygen abundances of these galaxies as a proxy for the metallicity, we first implement the so-called "direct" or T_e method, which requires a detection of the auroral [O III] λ4363 line as well as the [O III] $\lambda\lambda$4959, 5007 and [O II] λ3727 lines. Some of these lines lie in the UV/Visible at these redshifts, so we can only apply this method to the X-Shooter sample. Using the calibrations outlined in Izotov et al. (2006), we convert the [O III] emission-line ratios into an electron temperature (with the electron density constrained by the ratio of [O II] λ3729 to λ3726 or [S II] λ6717 to λ6731) in the O^{++} region. The total oxygen abundance in the galaxy is $O/H = O^{+}/H^{+} + O^{++}/H^{+}$, assuming $\log T_e(O^{+}) = 0.7 \log T_e(O^{++}) + 0.3$. Two objects, *UDS-12539* and *UDS-6377*, have detections of λ4363 and an upper limit can be obtained for a third,

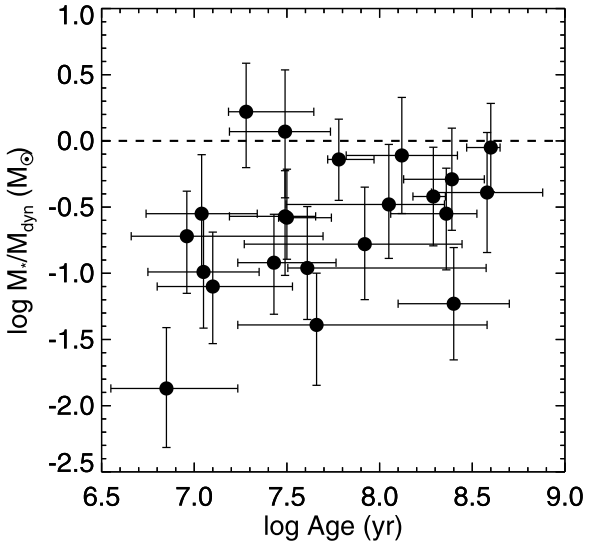

Figure 5. Ratio of stellar mass to total dynamical mass vs. age (mass-weighted) for the sample, with dynamical masses based on line measurements coming from the ground-based NIR spectra and stellar masses and ages from MAGPHYS.

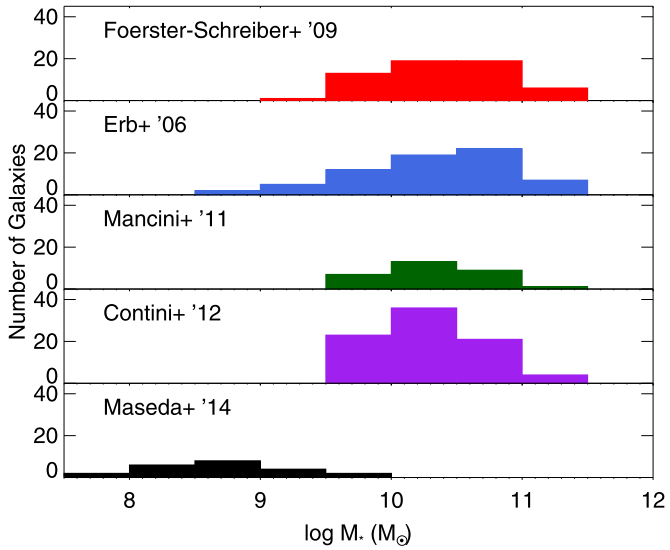

Figure 6. Histograms of stellar mass for our sample compared to the larger Hα samples of Förster-Schreiber et al. (2009), Erb et al. (2006), Mancini et al. (2011), and Contini et al. (2012) at $z > 1$. While variations in the stellar templates and the IMF used can alter stellar mass estimates by ∼0.3 dex, our sample still lies at considerably lower masses (up to two orders of magnitude lower) than the other samples.

(A color version of this figure is available in the online journal.)

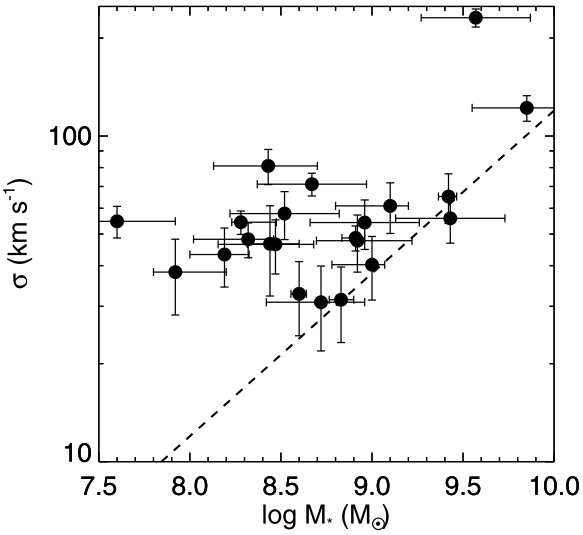

Figure 7. Stellar mass vs. observed line width for the sample. There is no clear trend of increasing line width with increasing stellar mass. The overplotted dashed line corresponds to $M_\star \sim M_{\rm virial}$ for a fixed $r_{\rm eff}$ of 1 kpc.

Table 4
Metallicity Estimates

ID	12 + log(O/H)	Method
GOODS-S-43693	8.10 ± 0.34	N2
GOODS-S-43928	7.70 ± 0.53	T_e/N2
UDS-6195	8.11 ± 0.23	O3N2
UDS-6377	7.52 ± 0.37	T_e
UDS-12539	7.45 ± 0.09	T_e
UDS-24154	8.25 ± 0.32	O3N2
COSMOS-19049	8.20 ± 0.20	N2

GOODS-S-43928. This object also lacks a detection of [O II]λ3727 due to skyline contamination, so the O^+/H^+ component cannot be constrained directly. The relative contribution of the O^+/H^+ component to the total oxygen abundance is 1.8% and 7.3% for the other two objects, so we neglect its contribution to the abundance of the third object. The N2 method of (Pettini & Pagel 2004, PP04), which uses the (log) ratio [N II] λ6584/Hα, verifies this result. All derived temperatures are in excess of 20,000 K.

For the remainder of the sample, we must resort to other methods, namely the aforementioned N2 method and also the O3N2 method, both from PP04; O3N2 is the (log) ratio [O III] λλ4959, 5007/Hβ/N2. For both methods, uncertainties include contributions from the error in the line ratios as well as the systematic scatter in the relations. If Hβ is not detected at more than 1σ in our LUCI1 or X-Shooter spectrum, we estimate the [O III]/Hβ ratio from the grism spectrum. Also note that in the two instances where the N2 method is used, the Maiolino et al. (2008) calibration results in metallicities consistent with the PP04 values. Results are displayed in Table 4, with a median 12 + log(O/H) value of 7.90 (0.15 $Z_\odot$). This value agrees well with the median MAGPHYS-derived metallicity of 0.17 $Z_\odot$ for the full sample.

Given the relatively small number of direct measurements of the oxygen abundance in high-z galaxies, this provides an important piece of information. Since the standard R23 diagnostic (Pagel et al. 1979) using [O III] λλ 4959, 5007 + [O II] λλ 3726, 3729 + Hβ is double-valued, it is important whether higher-z galaxies belong to the metal-rich upper branch or to the metal-poor lower branch. Henry et al. (2013a) argue in favor of the upper branch for galaxies with log $(M_\star/M_\odot) >$ 8.2 at $z \sim 0.7$, and Henry et al. (2013b) favor the upper branch for galaxies with log $(M_\star/M_\odot) > 8.8$ at $1.3 < z < 2.3$. Our measurements suggest that these systems plausibly lie on the lower branch, even at log $(M_\star/M_\odot) < 9.2$.

In the left panel of Figure 11 we show these results as well as those of Brammer et al. (2012b) and Erb et al. (2010) with the low-mass extrapolations to the mass–metallicity (MZ) relations from Kewley & Ellison (2008) for $z \sim 0.1$, Henry et al. (2013b) for emission line galaxies at $z \sim 1.8$, and Erb et al. (2006) for star-forming galaxies at $z \sim 2.2$ utilizing the metallicity

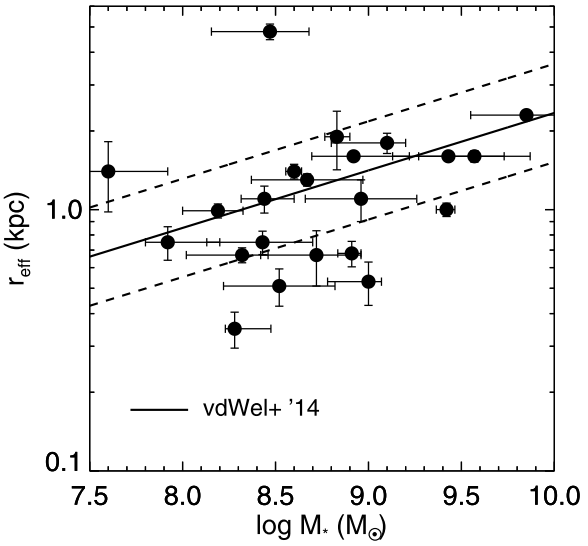

Figure 8. Effective radius vs. stellar mass for the sample. The overplotted lines are the low-mass extrapolation (and intrinsic scatter) to the relationship for star-forming galaxies at $2 < z < 2.25$ as found in van der Wel et al. (2014). The emission line galaxies in our sample fall on or somewhat below the size–mass relation for normal star-forming galaxies at similar redshifts.

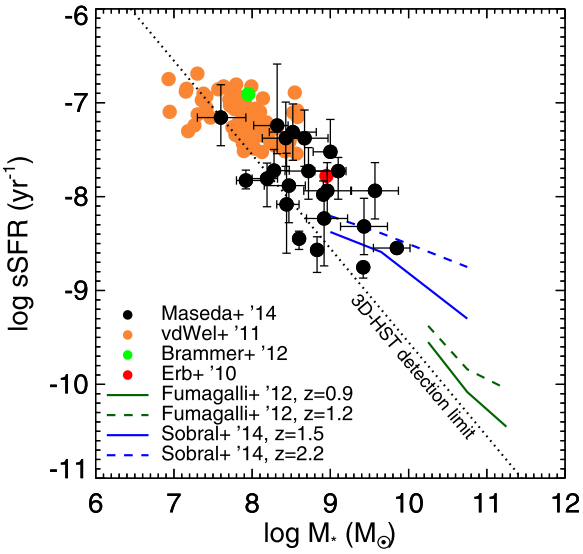

Figure 9. sSFR vs. stellar mass. Black points are the results from this study, orange points are the values from van der Wel et al. (2011), the red point is from Erb et al. (2010), the green point is from Brammer et al. (2012b), the blue lines are the results for the high/low-z bins of star-forming galaxies in Fumagalli et al. (2012), and the green lines are the results for the characteristic sSFR (SFR*/$M_\star$, see the text for details) for narrow-band selected star-forming galaxies in Sobral et al. (2014). The diagonal dotted line represents the nominal detection limit from the 3D-HST survey of 2.8 $M_\odot$ yr^{-1} at $z \sim 1.5$. The sSFRs are averaged over 10 Myr.

(A color version of this figure is available in the online journal.)

calibrations and functional parameterization of Maiolino et al. (2008), as well as the results from Amorín et al. (2010). The right panel of Figure 11 shows the same data plotted against the low-mass extrapolation of the "fundamental metallicity relation" (FMR) of Mannucci et al. (2010) and the relation for high-SFR galaxies at $z \sim 1.6$ from Zahid et al. (2013). Neither method is directly calibrated below $\sim 10^9$ $M_\odot$, which is precisely the range we probe here.

In the case of the MZ relation, our results generally agree with the Erb et al. (2006) and Henry et al. (2013b) extrapolations and typically have lower metallicities than objects with similar masses and SFRs at lower redshifts. We see good agreement with distribution in 12 + log(O/H) with $M_\star$ from Amorín et al. (2010) as well. The slight overall trend observed where higher-mass objects have higher metallicities supports the idea that the lowest-mass objects are the youngest and therefore have formed less mass of heavy elements. The youngest objects should also have the highest sSFRs, which is known to drive much of the scatter in the MZ relation. Henry et al. (2013a) also explain that the steepness of the O/H versus $M_\star$ relation has a direct theoretical impact on the role of outflows in these systems.

In the FMR relation, the solid points, denoting T_e-determined abundances, are considered more reliable at low metallicities (Maiolino et al. 2008) and lie somewhat below the FMR, perhaps more in line with an extrapolation to the $z \sim 1.6$ findings of Zahid et al. (2013). Since Mannucci et al. (2010) do not see the higher-mass turnoff in the relation until $z > 2.5$, we may be observing the evolution of the FMR on the low-mass and/or high-SFR end, although we do not have the number statistics yet to quantify any offset. At the very least, we can conclusively rule out that these objects lie above the FMR (see Stott et al. 2013, who claim this relation is driven by the higher average SFRs of the systems probed at higher redshifts).

5. CONSTRAINTS ON THE GAS FRACTION AND THE STAR FORMATION EFFICIENCY

In this section we use the observed velocity dispersions σ and sizes $r_{\rm eff}$, combined with dynamical stability criteria, to constrain the gas fraction and its implications. We assume that the systems consist entirely of stars and gas: we neglect the contribution of dark matter to the total dynamical mass as measured within the central kiloparsec. We also assume that these systems are isolated and not embedded in larger (gaseous) structures that exert pressure.

We do not know the geometry of the systems, and therefore consider two extreme cases: for the case of a sphere with uniform density we calculate the Jeans mass M_J; for the case of a thin rotating disk we calculate the Toomre parameter Q. In both cases we assume that the gaseous body has the same extent as the stellar body, and that the velocity width of the nebular lines traces the total gas kinematics.

For a uniform sphere, the Jeans mass (Binney & Tremaine 2008) is given by

$$M_J = \frac{4\pi}{3}\rho_0\left(\frac{\pi\sigma^2}{4G\rho_0}\right)^{3/2}, \quad (2)$$

where we have equated the sound speed with observed velocity dispersion. This velocity represents the combined effect of all sources of pressure that act against collapse, which include thermal motions (associated with the physical sound speed) as well as turbulence and streaming motions.

ρ_0 is the density of the gas, which is given by the gas mass ($f_{\rm gas} \times M_{\rm dyn}$) and the size

$$\rho_0 = \frac{f_{\rm gas} M_{\rm dyn}}{(4/3)\pi r_{\rm eff}^3}, \quad (3)$$

where $f_{\rm gas}$ is the gas fraction. The total dynamical mass $M_{\rm dyn}$ is taken from Equation (1), with a value of 5 for the proportionality

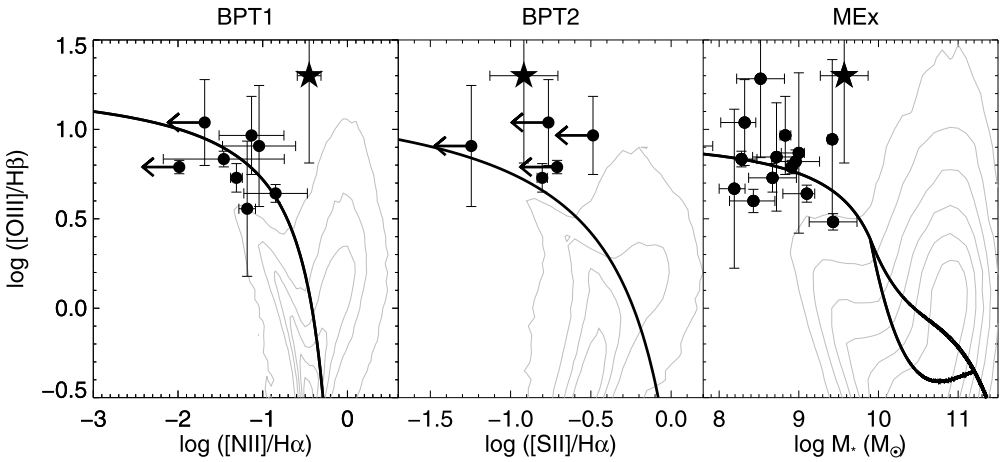

Figure 10. AGN/SF emission line diagnostic plots. From left to right, the BPT1 diagnostic of [N II] λ6584/Hα, the BPT2 diagnostic of [S II] λ6718+6731/Hα, and the MEx diagnostic (Juneau et al. 2011) of stellar mass. Divisions between the AGNs and the star-forming regions in the BPT diagrams come from Kewley et al. (2006). In all cases, the gray contours represent data from the SDSS MPA-JHU value-added DR7 catalog: these emission line and stellar mass measurements are described by Tremonti et al. (2004) and Kauffmann et al. (2003). Arrows denote 3σ upper limits. Each of the diagnostics point to star formation as the ionizing source with at most mild AGN contribution, the possible exception being *COSMOS-12102* (star symbol). The large uncertainties in [O III]/Hβ are caused by very low and uncertain Hβ fluxes, as [O III] is robustly detected in all of these cases; the true ratio could be even higher than the values plotted here.

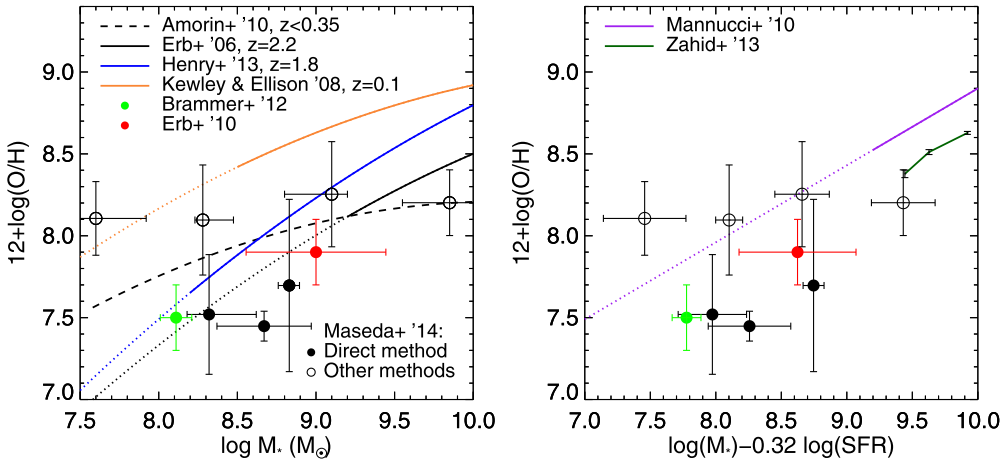

Figure 11. Left panel: oxygen abundances as a function of stellar mass. Overplotted are the MZ relations of Kewley & Ellison (2008), Henry et al. (2013b), and Erb et al. (2006) with low-mass extensions given as the dotted lines, using the Maiolino et al. (2008) parameterization. The dashed line is the Amorín et al. (2010) relation for luminous compact "green pea" galaxies at $0.11 < z < 0.35$. Right panel: oxygen abundances for our sample as a function of μ_{32} as defined in Mannucci et al. (2010), with the "FMRs" from Mannucci et al. (2010) and the high-SFR bin from Zahid et al. (2013) overplotted. In both panels, filled points denote abundances obtained from the "direct" T_e method and open points denote other methods. The red point shows the result from Erb et al. (2010) and the green point shows the result from Brammer et al. (2012b). Overall we observe that our objects lie on or below the low-mass/high-SFR extrapolations to these observed relationships at similar redshifts.

(A color version of this figure is available in the online journal.)

constant for consistency with the case under consideration here: that of a sphere with uniform density.[21]

For typical values of $r_{\rm eff}$ (1 kpc) and σ (50 km s^{-1}), we find that $M_J \simeq M_{\rm gas} (\equiv f_{\rm gas} M_{\rm dyn})$ for $f_{\rm gas} = 0.66$. Given that substantial star formation in these systems the gaseous body must be unstable: we conclude, assuming a homogeneous gaseous sphere, that $f_{\rm gas} \gtrsim 0.66$.

In order to address the question to what extent this conclusion is affected by the chosen geometry, we now consider the other (opposite) case, and assume that these systems are rotating disks, where instability can be described by the Toomre parameter Q (Toomre 1964; Binney & Tremaine 2008)

$$Q_{\rm gas} = \frac{\sigma_z \kappa}{\pi G \Sigma_{\rm gas}}, \quad (4)$$

where σ_z is the velocity dispersion perpendicular to the disk, and $\Sigma_{\rm gas}$ is the average gas-mass surface density, given by

$$\Sigma_{\rm gas} = \frac{M_{\rm gas}}{2\pi r_{\rm eff}^2} = \frac{M_{\rm dyn} f_{\rm gas}}{2\pi r_{\rm eff}^2}, \quad (5)$$

where $f_{\rm gas}$ is the gas fraction. The epicyclic frequency, κ, in a rotating exponential disk is

$$\kappa = \sqrt{2}(v_t / r_{\rm eff}), \quad (6)$$

where v_t is the circular velocity of the disk.

[21] Elsewhere in this paper we use a value of 3, which corresponds to other, more realistic geometries such as inclined disks and radially concentrated density profiles (e.g., isothermal).

While σ_z and v_t are not observed directly, both contribute to the observed linewidth, σ. The contribution of rotation to σ, assuming an average inclination of 60 degrees and an exponential disk, is $\sim v_{\rm rot}/\sqrt{2}$, such that we have

$$\sigma_{\rm obs}^2 = \sigma_z^2 + v_t^2/2, \quad (7)$$

which is empirically supported (Kassin et al. 2007).

Combining the above, we solve for v_t as a function of $\sigma_{\rm obs}$:

$$v_t^2 = \sigma_{\rm obs}^2 \left(1 \pm \sqrt{1 - (9/4) f_{\rm gas}^2 Q_{\rm gas}^2}\right), \quad (8)$$

such that an unstable system ($Q < 1$) requires

$$f_{\rm gas} > \tfrac{2}{3} \quad (9)$$

in order to produce a unique, physical solution.

Remarkably, regardless of whether we assume a homogeneous sphere or a rotating disk for the gas, we find that a high gas fraction is needed to explain the observed star formation activity. At the same time, the non-negligible contribution of the stellar mass to the total mass implies that $f_{\rm gas}$ cannot be arbitrarily close to unity and should be $\lesssim$0.9 (see Figure 5).

A significant caveat is that the proportionality constants in Equations (2), (3), (1), (6), (7), and (8) depend on the details of the assumed geometry and dynamical structure; their variation can alter the threshold value of $f_{\rm gas}$. In addition, we ignore the stabilizing effect of the stellar disk on the gas disk; however, this increases the implied gas fraction further.

The median gas fraction in our sample is 72% (i.e., the y-axis in Figure 5 is a proxy for $f_{\rm gas}$), in agreement with the theoretical calculation. While some objects are observed to have lower gas fractions, 18 out of our 22 objects are consistent with $f_{\rm gas} > 2/3$ within 1σ.

In the following we assume $f_{\rm gas} = 2/3$ in order to constrain the star formation efficiency. In Figure 12 we show the star formation rate surface density, assuming $\Sigma_{\rm SFR} = SFR/(2\pi \times r_{\rm eff})$, versus the gas surface mass density $\Sigma_{\rm gas}$ (from Equation (5)). The implied gas depletion timescale ranges from $\tau_{\rm depl} = 10^{7.5}$ to 10^9 yr, with a median of 3×10^8 yr.

Compared to normal present-day galaxies, gas is efficiently transformed into stars but, with the exception of a few objects, not as efficiently as observed in starbursting regions in the Milky Way and starbursting galaxies in the present-day or high-redshift universe (i.e., Kennicutt et al. 2007; Daddi et al. 2010). This mostly reflects the large gas fractions needed to produce systems that are unstable against star formation, rather than a modest level of star formation: the inverse sSFR (stellar mass growth timescale) of $1/{\rm sSFR} = 5 \times 10^7$ yr is very short, among the fastest ever measured. Hence, the stellar mass grows at a dynamical timescale ($\tau_{\rm dyn} \sim 3 \times 10^7$ yr).

The physical interpretation is that the SFR is not limited by availability of fuel but by the dynamical timescale. However, we have to keep in mind that we selected galaxies based on their sSFR: we are biased against objects that are older and/or have longer star formation timescales. Further empirical investigation of lower levels of star formation in similarly massive galaxies is needed to address this issue.

However, we propose that star formation will halt within ~50 Myr, long before the gas reservoir is depleted. First, the stability arguments given above imply that the gas fraction only needs to be reduced by a small amount (from the assumed $f_{\rm gas} = 2/3$ to, say, $f_{\rm gas} < 0.5$). Given the observed SFR, this takes ~50 Myr. Second, feedback should play an important role in these low-mass systems with small escape velocities (several 100 km s^{-1}) and high SFR: gas is easily transported out of the galaxy, and perhaps even out of the halo, preventing recycling. This paradigm is supported by Law et al. (2009, 2012), who see that higher-mass star-forming galaxies at $z \sim 2$ can support more extended rotationally supported disks and are less efficient at driving outflows than their lower-mass counterparts.

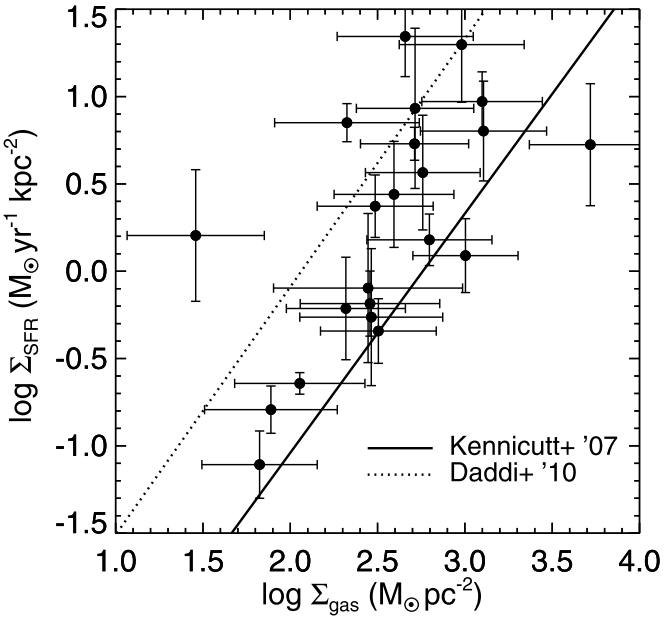

Figure 12. SFR surface density vs. gas-mass surface density. The gas masses are estimated according to $M_{\rm gas} = (2/3) \times M_{\rm dyn}$, which is inferred as a probable gas fraction given the star formation rates and $M_\star/M_{\rm dyn}$ ratios (which imply $0.5 \lesssim f_{\rm gas} \lesssim 0.9$) in these systems. The solid black line shows the relation for local spiral galaxies from Kennicutt et al. (2007) and the dotted line shows the result for local (U)LIRG and high-z SMGs/QSOs from Daddi et al. (2010). The location of the points suggests that these objects spend at least some of the time forming stars more efficiently than the normal, present-day spiral galaxies. Our constraints are not stringent enough to confirm or rule out gas depletion timescales that are on par with or even shorter than more massive, starbursting systems.

In the above we have ignored the infall of cold gas, which could continue to feed and maintain the starburst. Assuming that these galaxies reside in relatively low-mass halos ($\sim 10^{11}$ $M_\odot$) the typical accretion rate onto the halo is several $M_\odot$ yr^{-1} (McBride et al. 2009), somewhat lower than the SFR. The accretion rate onto the halo is not necessarily equal to the accretion rate onto the galaxy, and the latter is likely not constant. A period of above-average accretion for several 100 Myr could, in principle, sustain the starburst. However, above-average accretion events are more likely to be of short duration, such that one such event can ignite the observed starburst by pushing the gas mass surface density above the threshold for star formation or by disturbing the already-present gas, creating an instability. Hence, enhanced accretion could cause the star formation activity but not maintain it.

Based on the Jeans and Toomre instability arguments presented above, purely gaseous systems with velocity dispersions and sizes as observed become unstable once they reach a total mass of a few times 10^9 $M_\odot$, close to the observed masses of the objects in our sample.

6. SUMMARY

We presented near-infrared spectroscopy from the LBT/LUCI1 multi-object near-IR spectrograph and the VLT/X-Shooter wide band spectrograph for a sample of *HST*/WFC3 grism-selected emission line objects with restframe equivalent widths of EW = 200–1100 Å for [O III] λ5007 and/or Hα, and located in the redshift range $1.3 < z < 2.3$. The observed emission lines are narrow, with measured velocity dispersions down to $\sigma = 30$ km s^{-1}, implying low dynamical masses of $\sim 10^9$ $M_\odot$, even for the lower-EW objects not included in Maseda et al. (2013). Stellar masses determined using sophisticated MAGPHYS SED fitting to broadband magnitudes and the inclusion of line fluxes results in low stellar masses as well, $\sim 3 \times 10^8$ $M_\odot$. Ratios of $M_\star$ to $M_{\rm dyn}$ range from 1/10 to 1, which makes AGN-dominated SEDs unlikely. Emission-line ratios and the narrow line widths also suggest that AGNs do not significantly contribute to our sample, and therefore we conclude that the main ionizing source is hot, massive stars.

Direct probes of the oxygen abundances within these galaxies and [O III]/Hβ line ratios of typically $\gtrsim$5 corroborate the expectation that these low-mass systems have low metallicities, between 0.05 and 0.3 $Z_\odot$. They lie on or below the (extrapolated) mass–metallicity relationships for these redshifts (Henry et al. 2013b; Erb et al. 2006), which, combined with their young SED-derived ages, reinforces the notion that these are nascent galaxies undergoing their first major episode of star formation.

Measured sSFR values of $\sim 10^{-8}$ yr^{-1} for these galaxies are up to two orders of magnitude larger than those of typical 10^{10} $M_\odot$ star-forming galaxies at $z \gtrsim 1$ (Fumagalli et al. 2012), as well as comparable to or greater than the values from other high-EW systems as discovered in deep narrowband searches (Sobral et al. 2014) and in deep spectroscopic studies at both similar (Masters et al. 2014) and lower redshifts (Amorín et al. 2014a, 2014b). Such high sSFR values have been difficult to reproduce in hydrodynamical simulations, but recently Shen et al. (2013) made significant progress by combining a high gas density threshold for star formation and a blastwave scheme for supernova feedback in their simulations of low-mass galaxies.

Such low mass systems, with observed velocity dispersions of $\sigma \sim 50$ km s^{-1} and sizes of $\sim$1 kpc are only unstable against star formation if their gas fractions are high (above two-thirds), in agreement with the observed $M_\star/M_{\rm dyn}$ relation. The bursts are likely to be short-lived ($\sim$50 Myr), as, even in the absence of feedback, their intense star formation will rapidly build up stellar mass and lower their sSFR well before the gas depletion timescale ($\sim$100 Myr).

These results strengthen the conclusions from van der Wel et al. (2011), who argued that EELGs represent low-mass, starbursting galaxies. Additionally, the existence of (at least) two strong galaxy–galaxy lenses in the CANDELS/3D-HST fields where the background galaxy is an EELG at $z = 1.85$ and 3.42 (Brammer et al. 2012b; van der Wel et al. 2013, respectively) suggests that this type of object is common. The ubiquity of EELGs may be even more pronounced at high redshifts (>6; Smit et al. 2014). Such systems at $z = 1$–2 thus may present an opportunity to study how star formation proceeded in the early universe before the advent of the next generation of observatories, such as the *James Webb Space Telescope*.

The new generation of submillimeter observatories, such as ALMA, can provide direct estimates of the gas masses. Searching for the presence of outflowing material would provide valuable clues about the feedback processes going on in these systems, which is especially relevant to support the hypothesis that these bursts can create the cored dark matter profiles observed in local dwarf galaxies (e.g., Amorisco et al. 2014).

M.V.M. is a member of the International Max Planck Research School for Astronomy and Cosmic Physics at the University of Heidelberg, IMPRS-HD, Germany. C.P. acknowledges support by the KASI-Yonsei Joint Research Program for the Frontiers of Astronomy and Space Science funded by the Korea Astronomy and Space Science Institute. D.C.K. acknowledges funding from NSF grant AST-08-08133. We would also like to thank R. Amorín for productive discussions and C. Berlind and F. Rice for their computational expertise.

Facilities: LBT, VLT:Melipal, *HST*.

REFERENCES

Aird, J., Coil, A. L., Moustakas, J., et al. 2012, ApJ, 746, 90
Amorín, R. O., Pérez-Montero, E., Contini, T., et al. 2014a, arXiv:1403.3441
Amorín, R. O., Peréz-Montero, E., & Vílchez, J. M. 2010, ApJL, 715, L128
Amorín, R. O., Sommariva, V., Castellano, M., et al. 2014b, arXiv:1403.3692
Amorín, R. O., Vílchez, J. M., Hägele, G. F., et al. 2012, ApJL, 754, L22
Amorisco, N. C., Zavala, J., & de Boer, T. J. L. 2014, ApJL, 782, L39
Atek, H., Malkan, M., McCarthy, P., et al. 2010, ApJ, 723, 104
Atek, H., Siana, B., Scarlata, C., et al. 2011, ApJ, 743, 121
Baldwin, J., Phillips, M., & Terlevich, R. 1981, PASP, 93, 5
Binney, J., & Tremaine, S. 2008, Galactic Dynamics (2nd ed.; Princeton, NJ: Princeton Univ. Press)
Bouwens, R. J., Oesch, P. A., Illingworth, G. D., et al. 2013, ApJL, 765, L16
Brammer, G. B., van Dokkum, P., Franx, M., et al. 2012a, ApJS, 200, 13
Brammer, G. B., Sánchez-Janssen, R., Labbé, I., et al. 2012b, ApJL, 758, L17
Brammer, G. B., van Dokkum, P. G., Illingworth, G. D., et al. 2013, ApJL, 765, L2
Cardamone, C., Schawinski, K., Sarzi, M., et al. 2009, MNRAS, 399, 1191
Chabrier, G. 2003, PASP, 115, 763
Charlot, S., & Longhetti, M. 2001, MNRAS, 323, 887
Coe, D., Zitrin, A., Carrasco, M., et al. 2013, ApJ, 762, 32
Conroy, C. 2013, ARA&A, 51, 393
Contini, T., Garilli, B., Le Fevre, O., et al. 2012, A&A, 539A, 91
Curtis-Lake, E., McLure, R. J., Dunlop, J. S., et al. 2013, MNRAS, 429, 302
da Cunha, E., Charlot, S., & Elbaz, D. 2008, MNRAS, 388, 1595
da Cunha, E., Walter, F., Decarli, R., et al. 2013, ApJ, 765, 9
Daddi, E., Elbaz, D., Walter, F., et al. 2010, ApJL, 714, L118
Ellis, R. S., McLure, R. J., Dunlop, J. S., et al. 2013, ApJL, 763, L7
Erb, D. K., Pettini, M., Shapley, A. E., et al. 2010, ApJ, 719, 1168
Erb, D. K., Shapley, A. E., Pettini, M., et al. 2006, ApJ, 644, 813
Förster-Schreiber, N. M., Genzel, R., Bouché, N., et al. 2009, ApJ, 706, 1364
Fumagalli, M., Labbe, I., Patel, S., et al. 2013, ApJ, (arXiv:1308.4132)
Fumagalli, M., Patel, S. G., Franx, M., et al. 2012, ApJL, 757, L22
Gallagher, J. S., Hunter, D. A., & Tutukov, A. V. 1984, ApJ, 284, 544
Governato, F., Zolotov, A., Pontzen, A., et al. 2012, MNRAS, 422, 1231
Grebel, E. 1997, RvMA, 10, 29
Grogin, N., Kocevski, D., Faber, S., et al. 2011, ApJS, 197, 35
Groves, B. A., Heckman, T. M., & Kauffmann, G. 2006, MNRAS, 371, 1559
Henry, A., Martin, C. L., Finlator, K., & Dressler, A. 2013a, ApJ, 769, 148
Henry, A., Scarlata, C., Domínguez, A., et al. 2013b, ApJL, 776, L27
Izotov, Y. I., Guseva, N. G., & Thuan, T. X. 2011, ApJ, 728, 161
Izotov, Y. I., Stasińska, G., Meynet, G., et al. 2006, A&A, 448, 955
Izotov, Y. I., & Thuan, T. X. 2008, ApJ, 687, 133
Jones, T., Swinbank, A. M., Ellis, R. S., Richard, J., & Stark, D. P. 2010, MNRAS, 404, 1247
Juneau, S., Dickinson, M., Alexander, D. M., & Salim, S. 2011, ApJ, 736, 104
Karim, A., Schinnerer, E., Martínez-Sansigre, A., et al. 2011, ApJ, 730, 61
Kassin, S. A., Weiner, B. J., Faber, S. M., et al. 2007, ApJL, 660, L35
Kauffmann, G., Heckman, T. M., White, S. D. M., et al. 2003, MNRAS, 341, 33
Kennicutt, R. C., Jr., Calzetti , D., Walter, F., et al. 2007, ApJ, 671, 333
Kewley, L. J., & Ellison, S. L. 2008, ApJ, 681, 1183
Kewley, L. J., Groves, B., Kauffmann, G., & Heckman, T. 2006, MNRAS, 372, 961
Kewley, L. J., Maier, C., Yabe, K., et al. 2013, ApJL, 774, L10
Koekemoer, A., Faber, S., Ferguson, H., et al. 2011, ApJS, 197, 36
Law, D. R., Steidel, C. C., Erb, D. K., et al. 2009, ApJ, 697, 2057

Law, D. R., Steidel, C. C., Shapley, A. E., et al. 2012, ApJ, 756, 29
Lee, J. C., Kennicutt, R. C., José, G., et al. 2009, ApJ, 692, 1305
Maiolino, R., Nagao, T., Grazian, A., et al. 2008, A&A, 488, 463
Mancini, C., Förster-Schreiber, N. M., Renzini, A., et al. 2011, ApJ, 743, 86
Mannucci, F., Cresci, G., Maiolino, R., et al. 2010, MNRAS, 408, 2115
Maseda, M. V., van der Wel, A., da Cunha, E., et al. 2013, ApJL, 778, L22
Masters, D., McCarthy, P., Siana, B., et al. 2014, ApJ, 785, 153
Mateo, M. L. 1998, ARA&A, 36, 435
McBride, J., Fakhouri, O., & Ma, C.-P. 2009, MNRAS, 398, 1858
Navarro, J., Eke, V., & Frenk, C. 1996, MNRAS, 283, 72
Osterbrock, D. E., & Mathews, W. G. 1986, ARA&A, 24, 171
Pacifici, C., Charlot, S., Blaizot, J., & Brinchmann, J. 2012, MNRAS, 421, 2002
Pacifici, C., da Cunha, E., Charlot, S., et al. 2014, MNRAS, submitted
Pagel, B. E. J., Edmunds, M. G., Blackwell, D. E., Chun, M. S., & Smith, G. 1979, MNRAS, 189, 95
Pelupessy, F. I., van der Werf, P. P., & Icke, V. 2004, A&A, 422, 55
Pettini, M., & Pagel, B. E. J. 2004, MNRAS, 384, L59
Pontzen, A., & Governato, F. 2012, MNRAS, 421, 3464
Reines, A. E., Greene, J. E., & Geha, M. 2013, ApJ, 775, 116
Rix, H.-W., Guhathakurta, P., Colless, M., & Ing, K. 1997, MNRAS, 285, 779
Sargent, W. L. W., & Searle, L. 1970, ApJL, 162, L155
Seifert, W., Appenzeller, I., Baumeister, H., et al. 2003, Proc. SPIE, 4841, 962
Shen, S., Madau, P., Conroy, C., Governato, F., & Mayer, L. 2013, arXiv:1308.4131
Skelton, R. E., Whitaker, K. E., Momcheva, I. G., et al. 2014, ApJS, in press (arXiv:1403.3689)
Smit, R., Bouwens, R. J., Labbé, I., et al. 2014, ApJ, 784, 58
Sobral, D., Best, P. N., Smail, I., et al. 2014, MNRAS, 437, 3516
Stark, D. P., Schenker, M. A., Ellis, R. S., et al. 2013, ApJ, 763, 129
Stinson, G. S., Dalcanton, J. J., Quinn, T., et al. 2007, ApJ, 667, 170
Stott, J. P., Sobral, D., Bower, R., et al. 2013, MNRAS, 436, 1130
Straughn, A. N., Kuntschner, H., Kümmel, M., et al. 2011, AJ, 141, 14
Straughn, A. N., Meurer, G., Pirzkal, N., et al. 2008, AJ, 135, 1624
Swinbank, A. M., Sobral, D., Smail, I., et al. 2012, MNRAS, 426, 935
Toomre, A. 1964, ApJ, 139, 1217
Tremonti, C. A., Heckman, T. M., Kauffmann, G., et al. 2004, ApJ, 613, 898
Trump, J. R., Konidaris, N. P., Barro, G., et al. 2013, ApJL, 763, L6
Trump, J. R., Weiner, B. J., Scarlata, C., et al. 2011, ApJ, 743, 144
van der Wel, A., Bell, E., Häussler, B., et al. 2012, ApJS, 203, 24
van der Wel, A., Franx, M., van Dokkum, P. G., et al. 2014, ApJ, 788, 28
van der Wel, A., Straughn, A., Rix, H.-W., et al. 2011, ApJ, 742, 111
van der Wel, A., van de Ven, G., Maseda, M., et al. 2013, ApJL, 777, L17
van Dokkum, P., Brammer, G. B., Fumagalli, M., et al. 2011, ApJL, 743, L15
Vernet, J., Dekker, H., D'Odorico, S., et al. 2011, A&A, 536A, 105
Weisz, D., Dalcanton, J., Williams, B., et al. 2011, ApJ, 739, 5
Xue, Y. Q., Wang, S. X., Brandt, W. N., et al. 2012, ApJ, 758, 129
Zahid, H. J., Kashino, D., Silverman, J. D., et al. 2013, arXiv:1310.4950
Zolotov, A., Brooks, A. M., Willman, B., et al. 2012, ApJ, 761, 71